Symmetry and strain analysis of structural phase transitions in $Pr_{0.48}Ca_{0.52}MnO_3$

Michael A. Carpenter and Ruth E. A. McKnight
Department of Earth Sciences, University of Cambridge, Downing Street, Cambridge CB2 3EQ, United Kingdom

Christopher J. Howard
Department of Earth Sciences, University of Cambridge, Downing Street, Cambridge CB2 3EQ, United Kingdom and School of Engineering, University of Newcastle, University Drive, Callaghan, New South Wales 2308, Australia

Kevin S. Knight
ISIS Facility, Rutherford Appleton Laboratory, Chilton, Didcot, Oxfordshire OX11 0QX, United Kingdom
(Received 4 February 2010; revised manuscript received 28 June 2010; published 7 September 2010)

Structural evolution as a function of temperature through the *Pnma*↔incommensurate (IC) phase transition in $Pr_{0.48}Ca_{0.52}MnO_3$ perovskite has been analyzed from the perspectives of symmetry and strain. The structure and stability of both phases are shown to depend on combinations of order parameters which have symmetries associated with irreducible representations M_3^+, R_4^+, M_2^+, Γ_3^+ and Σ_2 of space group $Pm\bar{3}m$. The physical origin of these can be understood in terms of octahedral tilting, cooperative Jahn-Teller distortions and charge order/Zener polaron ordering. The M_2^+ order parameter describes the Jahn-Teller ordering scheme which develops in $LaMnO_3$ while the Γ_3^+ order parameter relates to an ordering scheme in which the unique axes of the distorted octahedra are all aligned in the same direction. Irrep Σ_2 contains two components with gradient coupling and provides the symmetry-breaking mechanism by which the IC transition can occur. Each order parameter couples with macroscopic spontaneous strains in a manner that depends strictly on symmetry and this leads to specific interactions between the order parameters through their coupling with common strains. In order to establish the extent and importance of this coupling, symmetry-adapted strains have been extracted from a new set of lattice parameters obtained by high-resolution powder neutron diffraction in the temperature interval 10–1373 K. It is found that the predominant strain of the incommensurate structure (up to ~2.5%) is a tetragonal shear strain which arises by bilinear coupling with the Γ_3^+ order parameter. This combination is probably responsible for most of the energy reduction accompanying the *Pnma*↔IC transition and also gives it some characteristics typical of a pseudoproper ferroelastic transition. Strain coupling promotes mean-field behavior and the evolution of the symmetry-breaking order parameter can be described by a standard Landau tricritical solution, $q^4 \propto (T_c - T)$ with $T_c = 237 \pm 2$ K. Octahedral tilting at high temperatures is closely similar to tilting in the *Pnma* structure of other perovskites, such as $SrZrO_3$. This is accompanied by a degree of Jahn-Teller ordering on the basis of the M_2^+ scheme below ~775 K but is replaced by the Γ_3^+ scheme below T_c. In contrast with the tilting and Jahn-Teller effects, magnetic ordering at the Néel temperature (~180 K) is accompanied by only the slightest volume strain and is not likely to influence the evolution of the other order parameters to any significant extent, therefore. An additional change in the volume strain below ~85 K is perhaps related to changes in magnetic structure at lower temperatures. Line broadening in powder diffraction patterns collected in the temperature interval ~150–260 K appears to be related to the presence of ferroelastic twins arising from octahedral tilting and draws attention to the fact that the *Pnma*↔IC transition takes place in a material which already contains heterogeneities. Finally, correlation of the repeat distance of the IC structure with Γ_3^+ distortions of MnO_6 octahedra shows that the nature of the IC structure itself is also determined essentially by geometrical factors and strain.

DOI: 10.1103/PhysRevB.82.094101 PACS number(s): 61.50.Ks, 61.05.fm, 61.44.Fw

I. INTRODUCTION

Intense interest in manganite perovskites over a prolonged period has focused substantially on the rich diversity of their electronic, electrical, and magnetic properties, including colossal magnetoresistance (CMR).[1–7] The local origin of the properties of interest lies in the electronic configuration of octahedrally coordinated Mn cations on crystallographic *B* sites while the diversity is induced largely by changing the average cation charge across solid solutions between end members nominally containing only Mn^{3+} or Mn^{4+}. Two common themes which permeate nearly all the analysis of structure/property relations of solid solutions such as $La_{1-x}Ca_xMnO_3$ and $Pr_{1-x}Ca_xMnO_3$ have been, first, competition between magnetic and structural instabilities[8–13] and, second, the role of strain.[10,12,14–21] If magnetic ordering dominates, a ferromagnetic structure develops, but if other structural instabilities dominate a commensurate or incommensurate superstructure may develop. The general phenomenology of this competition can be described by a single Landau expansion with only two order parameters[9,12] and the structural changes are accompanied by significant changes in lattice parameters.[22–24] In addition, the solid solutions appear to be susceptible to the development of magnetic and structural heterogeneities over length scales of a few unit cells to a few hundred angstroms, which must also be accompanied

to some extent by strain effects.[5–7,18,21,25–30] Thus, although the metallic/insulator conductivity, CMR and FM/AFM properties originate from the local electronic state of octahedral manganese, the overall pattern of stability fields for different phases and microstructure must be influenced, or even dominated by elastic relaxations.

There appear to be close parallels between the behavior of manganite solid solutions and the natural mineral solid solution, plagioclase feldspar ($Na_xCa_{1-x}Al_{2-x}Si_{2+x}O_8$), which have not been noticed in the physics literature. The plagioclase phase diagram contains stability fields for commensurate and incommensurate superstructures, and just as for the manganites, the **k** vector defining the incommensurate repeat varies systematically with composition and probably also with temperature.[31] Changing Al:Si content is analogous to the variable $Mn^{3+}:Mn^{4+}$ ratio and competition is between different Al/Si ordering schemes rather than different electronic configurations. The framework structure also undergoes displacive phase transitions, analogous to octahedral tilting, which couple with the order parameters for Al/Si ordering. Furthermore, natural samples of plagioclase feldspars contain a diversity of characteristic microstructures on an electron optical scale due to separation between phases with different states of Al/Si order. In this specific case and for framework silicate minerals more generally, structural evolution is determined by coupling of multiple order parameters with strain.[31–33] Given this experience, without the complication of any electronic effects, the question then arises as to whether the overall behavior of manganite perovskites could likewise be understood simply in terms of order parameter coupling via common elastic strains.

The primary objective of the present work was to undertake a high-resolution strain analysis of the structural evolution of $Pr_{0.48}Ca_{0.52}MnO_3$, using a new set of lattice parameters extracted from neutron powder-diffraction data. If the initial premise of a predominant role for strain coupling is correct, it should be possible, first, to interpret the structural evolution with temperature in terms of specific symmetry-adapted strains and their coupling to specific macroscopic order parameters and, second, to show that this evolution conforms to standard solutions from Landau theory. The basis of this approach has been reviewed at length by Carpenter *et al.*[33] and developed further for pure tilting transitions in $NaTaO_3$, $(Ca,Sr)TiO_3$, and $SrZrO_3$ perovskites.[34–37] Coupling of tilting transitions with cation ordering has been treated for the case of $La_{2/3}TiO_3$ (Ref. 38) and with a Jahn-Teller transition for the case of $PrAlO_3$.[39] A comprehensive treatment of coupling between octahedral tilting and cooperative Jahn-Teller transitions is given by Carpenter and Howard,[40,41] to which cation ordering has been added by Howard and Carpenter.[42]

The choice of starting material was determined by the fact that a great deal is already known about the temperature dependence of the structure and properties of $Pr_{0.48}Ca_{0.52}MnO_3$. It is in the part of the $Pr_{1-x}Ca_xMnO_3$ phase diagram dominated by the stability of the incommensurate structure below ~250 K (Refs. 43–46) and undergoes an antiferromagnetic transition near 180 K.[23,43,47,48] Magnetization, heat-capacity variations, the evolution of the incommensurate **k** vector and its microstructure have been described by Cox *et al.*[20,49] and Sánchez *et al.*[50] These properties are closely similar to those reported for $Pr_{0.5}Ca_{0.5}MnO_3$, for which there are electrical resistivity, magnetic order, lattice parameter, x-ray resonance and ^{17}O NMR data,[23,45,46,51–55] together with information on the effect of grain size on some of these properties.[56,57] An important difference, however, is that $Pr_{0.5}Ca_{0.5}MnO_3$ is only incommensurate from ~240 K down to ~215 K where it transforms to a commensurate structure.[52]

The rest of this paper is divided into four main sections. First the symmetry changes which accompany transitions in $Pr_{0.48}Ca_{0.52}MnO_3$ are analyzed in terms of all possible order parameters, their irreducible representations and coupling with symmetry-adapted strains (Sec. II). The next two Secs. III and IV describe high-resolution powder neutron-diffraction methodologies and results. The discussion (Sec. V) draws together the overall implications of coupling between the individual order parameters whose evolution is extracted from the formal symmetry and strain analysis.

II. SYMMETRY ANALYSIS

A formal analysis of symmetry, in terms of irreducible representations, order-parameter components, and symmetry-breaking strains is developed here to identify constraints on the thermodynamic character of the $Pnma \leftrightarrow$ IC phase transition and to characterize permitted coupling between the order parameter components and symmetry-adapted strains. Use has been made throughout of the group theory program ISOTROPY.[58] It should be noted that ISOTROPY uses $Pmn2_1$ as the standard setting for space group number 31. It is convenient to rotate the crystallographic axes to the $Pnm2_1$ setting which is used in the literature to describe the commensurate equivalent of the incommensurate manganite structure.

A. *Pnma* reference structure

The high-temperature structure of $Pr_{1-x}Ca_xMnO_3$ has space group *Pnma*, and the IC structure which develops in crystals with a range of compositions at low temperatures is associated with the X point of the Brillouin zone. There are three possible symmetry subgroups associated with the relevant irrep, $X_1:P2_1/m$, $Pnm2_1$, or Pm (Table I, and see Refs. 30, 42, and 59–62). Odd order terms in the order parameter(s) are not permitted in the Landau free energy expansion for the transition to any of these. Gradient terms are permitted, however, such that the Lifshitz condition is violated and the phase transition is therefore required to be first order. The commensurate phase of $Bi_{0.6}Ca_{0.4}MnO_3$ has space group $Pnm2_1$ (Ref. 62) and displays abrupt changes in properties plus hysteresis at its $Pnma \leftrightarrow Pnm2_1$ transition, consistent with the expected first-order character. The related incommensurate structure of $La_{1-x}Ca_xMnO_3$ and $Pr_{1-x}Ca_xMnO_3$ has critical points away from the X point (along the Σ line of symmetry), however, and the weak Lifshitz condition for second-order character is no longer violated.[63] As a result, the $Pnma \leftrightarrow$ IC transition can be thermodynamically continuous. For the specific case of $Pr_{0.48}Ca_{0.52}MnO_3$, Cox *et al.*[49] have recently argued that available experimental data are

TABLE I. Subgroups of space group *Pnma* associated with irrep X_1.

Parent	Subgroup	Order-parameter components	Basis vectors	Origin
Pnma	$P2_1/m$	$(a,0)$	(2,0,0),(0,1,0),(0,0,1)	(1/2,0,0)
Pnma	$Pnm2_1$ [a]	(a,a)	(2,0,0),(0,1,0),(0,0,1)	(3/4,1/4,0)
Pnma	*Pm*	(a,b)	(2,0,0),(0,1,0),(0,0,1)	(1/4,0,0)

[a]ISOTROPY gives the space group for order-parameter components (a,a) in the standard setting, $Pmn2_1$. It is convenient in this work to reset this to $Pnm2_1$ $(\mathbf{a},\mathbf{b},\mathbf{c}\rightarrow\mathbf{b},\mathbf{a},-\mathbf{c})$ to maintain correspondence with the *Pnma* structure from which it is derived.

consistent with a continuous transition. These authors noted, in particular, that they were not able to detect any latent heat and that previously reported hysteresis which had been used to infer first-order character is due to kinetic constraints on the adjustment of the incommensurate repeat distance during heating and cooling. Evidence from transmission electron microscopy for multiple phases of $Pr_{0.5}Ca_{0.5}MnO_3$ coexisting over a wide temperature interval (between at least 80 and 300 K) has been interpreted as evidence for first-order character[30,64] but is contradicted by the continuous variation in the intensity of a superlattice reflection at the transition temperature of ~240 K.[52]

Symmetry subgroups of space group *Pnma* associated with irrep X_1 can have up to two order parameter components, q_1 and q_2. These are identical in $Pnm2_1$ (a,a) but differ in *Pm* (a,b), as shown in Table I. From ISOTROPY (and see, also, Ref. 9), the lowest order permitted gradient terms are $q_1\frac{\partial q_2}{\partial x}-q_2\frac{\partial q_1}{\partial x}$, where x is the direction of the crystallographic x axis of the *Pnma* and $Pnm2_1$ unit cells. Gradient coupling of this type is well known to be a mechanism for stabilizing incommensurate structures, whereas the previously accepted space group of $P2_1/m$ (Ref. 65 and many subsequent studies) has only one nonzero order-parameter component and, presumably, no gradient coupling of this type.

B. $Pm\bar{3}m$ reference structure

The *Pnma* perovskite structure arises by octahedral tilting associated with M and R points of the Brillouin zone of space group $Pm\bar{3}m$. Order parameters associated with irreps M_3^+ and R_4^+ would normally be described as primary, and the combination $M_3^+\oplus R_4^+$ leads to additional order parameters which would be referred to as being secondary. The full list of irreps for all possible order parameters arising at the $Pm\bar{3}m\rightarrow Pnma$ transition is given in Table II. In a perovskite with *B* site cations which have Jahn-Teller instabilities, additional structural distortions are associated with Γ_3^+ and M_2^+. The Γ_3^+ distortion can be understood in terms of a uniaxial distortion of individual octahedra with the unique axis of each lined up parallel to [010] of the *Pnma* lattice. The M_2^+ distortion can be understood as ordering of uniaxially distorted octahedra such that the unique axes alternate in their orientation within (010) planes.[40,41]

The X point of the Brillouin zone of space group *Pnma* is the point $(\frac{1}{4},\frac{1}{4},0)$ on the Σ line for space group $Pm\bar{3}m$, and there are four 12-dimensional irreps, Σ_1, Σ_2, Σ_3, and Σ_4, associated with points on this line.[42] Within the *Pnma* tilt system, atomic displacements associated with Σ_1 and one nonzero order-parameter component give the structure with space group $P2_1/m$ whereas Σ_1 or Σ_2 with two nonzero order-parameter components give space group $Pnm2_1$. Goff and Attfield[61] obtained a better fit to x-ray and neutron powder-diffraction data for $Pr_{0.5}Ca_{0.5}MnO_3$ under space group $P2_1/m$, but electron-diffraction results favor $Pnm2_1$.[30,64] On this basis the structural evolution of $Pr_{0.48}Ca_{0.52}MnO_3$ can be interpreted in terms of coupling between order parameter components belonging to Σ_1 or Σ_2 and components from M_3^+ and R_4^+ which relate to octahedral tilting. Combination of these irreps again leads to a number of additional order parameters with different symmetries so that, in principle, the complete evolution from $Pm\bar{3}m$ to $Pnm2_1$ can be broken down into the separate contributions listed in Table III. Γ_3^+ and M_2^+ Jahn-Teller ordering schemes are retained from $M_3^+\oplus R_4^+$. As an aside, it can be noted that the possibility of ferroelectric properties[30,64,66,67] arises from displacements associated with Γ_4^- and Γ_5^-.

Irreps Σ_1 and Σ_2 are also associated with two of the different models for ordering in manganites which have recently been proposed. The two order-parameter components of Σ_1 would give the bistripe pattern of charge order suggested for $Bi_{1-x}Sr_xMnO_3$ phases[68,69] (and see Refs 42 and 70). The two order-parameter components of Σ_2 give a pattern of displacements that matches the ordered Zener polaron model suggested for $Pr_{1-x}Ca_xMnO_3$.[30,42,59–61,64,66] In the ab-

TABLE II. Component subgroups, irreps, and order-parameter components of space group *Pnma* with respect to the parent supergroup $Pm\bar{3}m$. Basis vectors for the *Pnma* product are (0,1,1), (2,0,0), $(0,1,-1)$, and the origin is (0,0,0).

Irrep	Order-parameter components	Subgroup
Γ_1^+	(a)	$Pm\bar{3}m$
Γ_3^+	$(a,\sqrt{3}a)$	$P4/mmm$
Γ_5^+	$(0,a,0)$	*Cmmm*
R_4^+	$(a,0,a)$	*Imma*
R_5^+	$(a,0,-a)$	*Imma*
X_5^+	$(0,0,0,0,0,a)$	*Cmcm*
M_2^+	$(0,a,0)$	$P4/mbm$
M_3^+	$(0,a,0)$	$P4/mbm$

TABLE III. Component subgroups, irreps, and order-parameter components of space group $Pnm2_1$ with respect to the parent supergroup $Pm\bar{3}m$. The lattice vectors of $Pnm2_1$ with respect to $Pm\bar{3}m$ are (0,2,2), (2,0,0), (0,1,−1), and the origin is taken at (1/2,3/4,3/4).

Irrep	Order parameter components	Subgroup	Lattice vectors
Γ_1^+	(a)	$Pm\bar{3}m$	(1,0,0),(0,1,0),(0,0,1)
Γ_3^+	$(a,\sqrt{3}a)$	$P4/mmm$	(0,1,0),(0,0,1),(1,0,0)
Γ_5^+	$(0,a,0)$	$Cmmm$	(0,1,1),(0,−1,1),(1,0,0)
Γ_4^-	$(0,a,-a)$	$Amm2$	(1,0,0),(0,1,1),(0,−1,1)
Γ_5^-	$(a,0,a)$	$Amm2$	(1,0,0),(0,1,1),(0,−1,1)
Σ_1	$(0,0,0,0,0,0,0,0,a,a,0,0)$	$Pmma$	(0,−1,1),(1,0,0),(0,2,2)
Σ_2	$(0,0,0,0,0,0,0,0,a,-a,0,0)$	$Pbam$	(0,2,2),(0,−1,1),(1,0,0)
R_4^+	$(a,0,a)$	$Imma$	(0,1,1),(2,0,0),(0,1,−1)
R_5^+	$(a,0,-a)$	$Imma$	(0,1,1),(2,0,0),(0,1,−1)
R_2^-	(a)	$Fm\bar{3}m$	(2,0,0),(0,2,0),(0,0,2)
R_3^-	$(a,\sqrt{3}a)$	$I4/mmm$	(0,1,1),(0,−1,1),(2,0,0)
R_4^-	$(0,a,0)$	$I4/mmm$	(0,1,1),(0,−1,1),(2,0,0)
X_5^+	$(0,0,0,0,0,a)$	$Cmcm$	(0,1,−1),(0,1,1),(2,0,0)
X_1^-	$(0,0,a)$	$P4/mcc$	(0,1,0),(0,0,1),(2,0,0)
X_4^-	$(0,0,a)$	$P4_2/mmc$	(0,1,0),(0,0,1),(2,0,0)
M_2^+	$(0,a,0)$	$P4/mbm$	(0,1,1),(0,−1,1),(1,0,0)
M_3^+	$(0,a,0)$	$P4/mbm$	(0,1,1),(0,−1,1),(1,0,0)
M_5^-	$(0,0,0,0,a,0)$	$Pmma$	(0,−1,1),(1,0,0),(0,1,1)
S_3	$(0,0,0,0,a,-a,0,0,0,0,0,0)$	$Cmcm$	(2,0,0),(0,2,2),(0,−1,1)
S_4	$(0,0,0,0,a,a,0,0,0,0,0,0)$	$Cmca$	(2,0,0),(0,2,2),(0,−1,1)

sence of tilting, the Zener polaron ordering arrangement would have space group *Pbam*. Both Σ_1 and Σ_2 irreps are allowed in space group $Pnm2_1$ (Table III), however, and their relative importance cannot be distinguished in the present context.

Gradient terms generated using ISOTROPY and combinations of the order-parameter components listed in Table III are due to irreps Σ_1, Σ_2, S_3, and S_4. Terms for Σ_1 and Σ_2 have the form $q_1(\frac{\partial}{\partial Y}+\frac{\partial}{\partial Z})q_2-q_2(\frac{\partial}{\partial Y}+\frac{\partial}{\partial Z})q_1$, where q_1 and q_2 represent the two nonzero order-parameter components, and Y, Z are the reference axes to which the crystallographic axes of *Pnma* and $Pnm2_1$ structures are referred (Fig. 1). Gradient terms for S_3 and S_4 have the same form but these have not previously been considered and it is not clear that they would contribute differently to the stability of the IC structure.

C. Symmetry-adapted strains

Variations in order parameters associated with irreps M_3^+, R_4^+, Σ_2, Γ_3^+, and M_2^+ can be evaluated through their coupling with symmetry-adapted strains, as obtained from high-resolution lattice parameter data. Σ_1 could, alternatively, be used in place of Σ_2. Γ_1^+ and Γ_3^+ strains are defined in terms of linear strains, e_1, e_2, and e_3, parallel to axes X, Y, and Z of the orthogonal reference system, in the usual way[33] as

$$e_a = e_1 + e_2 + e_3 \quad (\Gamma_1^+), \tag{1}$$

$$e_{tz} = \frac{1}{\sqrt{3}}(2e_3 - e_1 - e_2) \quad (\Gamma_3^+), \tag{2}$$

$$e_{oz} = (e_1 - e_2) \quad (\Gamma_3^+) \tag{3}$$

Γ_5^+ strains are e_6, e_4, and e_5. For the specific case of the two components of Γ_3^+ being related as $(a,\sqrt{3}a)$ Eqs. (2) and (3) can be rewritten as

$$e_{tx} = \frac{1}{\sqrt{3}}(2e_1 - e_2 - e_3), \tag{4}$$

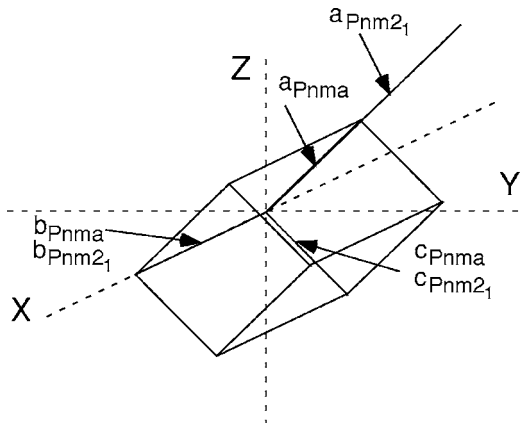

FIG. 1. Relationship between unit-cell axes for *Pnma* and $Pnm2_1$ structures and reference axes X, Y, and Z.

$$e_{ox} = (e_2 - e_3) = 0. \tag{5}$$

Subscripts t and o refer to tetragonal and orthorhombic strains while subscripts z and x specify the unique tetragonal axis as being along Z or X. The orientation of *Pnma* and $Pnm2_1$ unit cell axes with respect to this coordinate system are shown in Fig. 1. Both have $e_a \neq 0$, $e_{tx} \neq 0$, $e_4 \neq 0$, and $e_{ox} = e_5 = e_6 = 0$.

General expressions for strain coupling to order-parameter components associated with irreps M_3^+ and R_4^+ have been set out in full elsewhere,[35,37,71] as have expressions for order-parameter components associated with Γ_3^+ and M_2^+.[40] Irrep Σ_2 has 12 components ($q_{\Sigma 2,1}$ to $q_{\Sigma 2,12}$), and general expressions for coupling with strain are rather long. Only the case of special interest is considered here, which has $q_{\Sigma 2} = q_{\Sigma 2,9} = q_{\Sigma 2,10} \neq 0$, and $q_{\Sigma 2,1}$ to $q_{\Sigma 2,8} = q_{\Sigma 2,11} = q_{\Sigma 2,12} = 0$ (Table III). The lowest order strain coupling terms are $\lambda_{a\Sigma 2}(q_{\Sigma 2,9}^2 + q_{\Sigma 2,10}^2)e_a$, $\lambda_{t\Sigma 2}(q_{\Sigma 2,9}^2 + q_{\Sigma 2,10}^2)(\frac{\sqrt{3}}{2}e_{tz} - \frac{1}{2}e_{oz})$, $\lambda_{e1\Sigma 2}(q_{\Sigma 2,9}^2 + q_{\Sigma 2,10}^2)e_4$, $\lambda_{e2\Sigma 2}(q_{\Sigma 2,9}^2 + q_{\Sigma 2,10}^2)(e_5^2 + e_6^2)$, which give the following strain/order-parameter relationships:

$$e_a = \frac{-2\lambda_{a\Sigma 2} q_{\Sigma 2}^2}{\frac{1}{3}(C_{11}^o + 2C_{12}^o)}, \tag{6}$$

$$e_{tx} = \frac{2\sqrt{3}\lambda_{t\Sigma 2} q_{\Sigma 2}^2}{\frac{1}{2}(C_{11}^o - C_{12}^o)}, \tag{7}$$

$$e_4 = \frac{-2\lambda_{e1\Sigma 2} q_{\Sigma 2}^2}{C_{44}^o}. \tag{8}$$

C_{ik}^o are elastic constants of the cubic parent structure.

With respect to the cubic parent structure, the total strain contributions of M_3^+, R_4^+, Σ_2, Γ_3^+, and M_2^+ order parameters to the nonzero spontaneous strains of the $Pnm2_1$ structure are then

$$e_a = -\left[\frac{\lambda_1 q_2^2 + 2\lambda_2 q_4^2 + \lambda_{aM2+} q_{JT}^2 + \lambda_{a\Gamma 3+} q_{tx}^2 + 2\lambda_{a\Sigma 2} q_{\Sigma 2}^2}{\frac{1}{3}(C_{11}^o + 2C_{12}^o)}\right], \tag{9}$$

$$e_{tx} = -\left[\frac{2(\lambda_3 q_2^2 - \lambda_4 q_4^2) + 2\lambda_{tM2+} q_{2JT}^2 + \lambda_{t\Gamma 3+} q_{tx} - 2\sqrt{3}\lambda_{t\Sigma 2} q_{\Sigma 2}^2}{\frac{1}{2}(C_{11}^o - C_{12}^o)}\right], \tag{10}$$

$$e_4 = -\left[\frac{\lambda_5 q_4^2 + \lambda_{eM2+M3+} q_{2JT} q_2 + 2\lambda_{e1\Sigma 2} q_{\Sigma 2}^2}{C_{44}^o}\right]. \tag{11}$$

Labeling of the order parameter components and coupling coefficients follows the scheme used by Carpenter *et al.*[35,39] and Carpenter and Howard:[40] q_2 relates to M-point tilting, q_4 to R-point tilting, while q_{tx} and q_{2JT} represent Γ_3^+ and M_2^+ Jahn-Teller distortions, respectively. Following Carpenter[71] and Carpenter and Howard,[40] it has also been assumed that the magnitude of terms of the form $\lambda q_{tx} e_4^2$, $\lambda q_2^2 e_4^2$, and $\lambda q_{2JT}^2 e_4^2$ are small in comparison with $\frac{1}{2}C_{ik}^o e_4^2$.

Finally, these strain variations are determined directly from the variations of lattice parameters according to

$$e_1 = \frac{\frac{b_{Pnma}}{2} - a_o}{a_o}, \tag{12}$$

$$e_2 + e_3 = \frac{\frac{a_{Pnma}}{\sqrt{2}} - a_o}{a_o} + \frac{\frac{c_{Pnma}}{\sqrt{2}} - a_o}{a_o}, \tag{13}$$

$$e_4 = \frac{\frac{a_{Pnma}}{\sqrt{2}} - a_o}{a_o} - \frac{\frac{c_{Pnma}}{\sqrt{2}} - a_o}{a_o} \tag{14}$$

for the *Pnma* structure and

$$e_1 = \frac{\frac{b_{Pnm21}}{2} - a_o}{a_o}, \tag{15}$$

$$e_2 + e_3 = \frac{\frac{a_{Pnm21}}{2\sqrt{2}} - a_o}{a_o} + \frac{\frac{c_{Pnm21}}{\sqrt{2}} - a_o}{a_o}, \tag{16}$$

$$e_4 = \frac{\frac{a_{Pnm21}}{2\sqrt{2}} - a_o}{a_o} - \frac{\frac{c_{Pnm21}}{\sqrt{2}} - a_o}{a_o} \tag{17}$$

for the $Pnm2_1$ structure. The reference parameter, a_o, is that of the cubic phase extrapolated from its stability field at high temperatures.

III. EXPERIMENTAL METHODS

A. Sample preparation

Stoichiometric $Pr_{0.48}Ca_{0.52}MnO_3$ powder was purchased from Pi-Kem Ltd. It had been synthesized from raw materials with 99.9% purity and came with a reported average grain size of 0.7 μm. Three pellets of the powder, each weighing ~5 gm, were prepared by pressing for ~5 min in a standard cylindrical IR pellet die (diameter 13 mm) with a load of ~31 MPa under a vacuum generated by a rotary pump. The pellets were heated in air from room temperature to 900 °C at 1 °C min^{-1}, then from 900 to 1360 °C at 0.5 °C min^{-1}, followed by an annealing period of 48 h at 1360 °C and subsequent cooling back to room temperature at 0.5 °C min^{-1}. According to the results of Podzorov *et al.*[72] for $(La,Pr,Ca)MnO_3$, this heat treatment would be expected to give grain sizes of ~5–15 μm. The fired pellets were crushed and ground by hand in an agate mortar and pestle under acetone for a total of 1–2 h. The resultant powder was passed through a 250 μm sieve.

B. Neutron diffraction

Approximately 13.5 g of $Pr_{0.48}Ca_{0.52}MnO_3$ powder was loaded into a 10-mm-thick aluminum slab can that also housed a heater and Rh/Fe sensor. A neutron-absorbing gadolinium mask was attached with a view to minimizing contaminant Bragg peaks from either the body of the sample can, including sensor and heater, or the stainless steel frames supporting the vanadium windows. The assembly was mounted on a center stick and then cooled in a Sumitomo 415 closed cycle refrigerator with 60–80 mbars of He exchange gas. The sequence of data collection started with manual control of temperature for 5, 10, and 15 K, with ~5 min equilibration time at each temperature. Automatic data collection proceeded in a heating sequence starting at 20 K, with 5 K steps up to 490 K. Again, a period of 5 min was allowed for thermal equilibration at each temperature. Diffraction patterns were recorded in the three detector banks for a total incident proton beam of 9 μA h, corresponding to approximately 15 min. At 50 K intervals, the data collection time for individual spectra was extended to a total incident proton beam of 34 μA h.

For data collection at higher temperatures, the same sample was loaded into an 11 mm diameter vanadium sample can, which was mounted in an RAL vacuum furnace with vanadium heating elements. Thermometry was based on type *K* thermocouples positioned in contact with the sample can at about 20 mm above the beam center. All higher temperature patterns were recorded to a total incident proton beam of 8 μA h. There were in fact two sessions of measurements at furnace temperatures. In the first of these, the first pattern was recorded in the furnace at room temperature (293 K), the second was recorded at 370 K after equilibration at that temperature for an hour, the third at 470 K after 40 min equilibration, then to 625 K in 5 K steps, and finally from 650 K to 1175 K in 25 K steps, with 5 min prior equilibration in each case. After another room-temperature collection, the sample was heated to 1373 K where it was allowed to equilibrate for 30 min before the first diffraction pattern was collected. Further patterns were collected at 1373 K then at 10 K intervals during a cooling sequence down to 1073 K, with 5 min thermal equilibration at each temperature step. The sample was cooled to room temperature and a final pattern recorded. It emerged as a very slightly sintered black powder.

All diffraction patterns were recorded over the time-of-flight range 30–130 ms, corresponding to a *d*-spacing range 0.6–2.6 Å or 0.9–3.7 Å for patterns collected in the backscattering and ninety degree detector banks respectively. The patterns were normalized and corrected for detector efficiency according to prior calibration with a vanadium scan. Lattice parameters and atomic coordinates were refined from the diffraction patterns using the Rietveld method, as implemented in the GSAS computer program.[73] From an inspection of these diffraction patterns it seemed reasonable to assume a *Pnma* starting structure for the low temperature and the first of the high-temperature runs whereas for the analysis of the patterns recorded in the second high-temperature run a starting structure in $R\bar{3}c$ appeared to be a more appropriate choice. Patterns from the backscattering and 90° banks were fitted simultaneously, the diffractometer constant for the 90° bank being released to ensure that the lattice parameters were determined by the higher resolution backscattering bank in every case. Peak shapes were modeled as convolutions of back-to-back exponentials with pseudo-Voigt functions in which two peak width parameters (or three such parameters for the 90° data) were varied and the background as six-parameter shifted Chebyshev polynomials. Internal coordinates were refined along with displacement parameters, the oxygen displacement parameters being taken to be anisotropic.

IV. EXPERIMENTAL RESULTS

A. Structural data

Refinements from diffraction data collected below ~250 K using *Pnma* symmetry to represent the average structure accounted successfully for all the main diffraction peaks. Additional weak reflections, which are of magnetic origin (vanished at ~150 K), or attributable to the incommensurate superstructure (did not index on a commensurate cell and vanished at ~250 K), as expected on the basis of previous studies of this system, were found in the patterns recorded to higher statistics (i.e., to 34 μA h). Even in these patterns the number and intensities of superstructure reflections was considered to be insufficient to support refinement in any symmetry lower than *Pnma*. There were, in addition, weak residual contaminants that persisted throughout the cryostat run. The weak contaminant reflections aside, diffraction patterns collected in the temperature interval ~250–1175 K, which includes overlap between data from two different sample holders and heating/cooling systems, were refined successfully as a single homogenous *Pnma* phase. The room-temperature pattern collected after cooling from the peak of 1175 K differed from the room-temperature spectrum collected at the start in having smaller splittings of major peaks and weaker M-point reflections, which is interpreted as implying some minor change in stoichiometry due

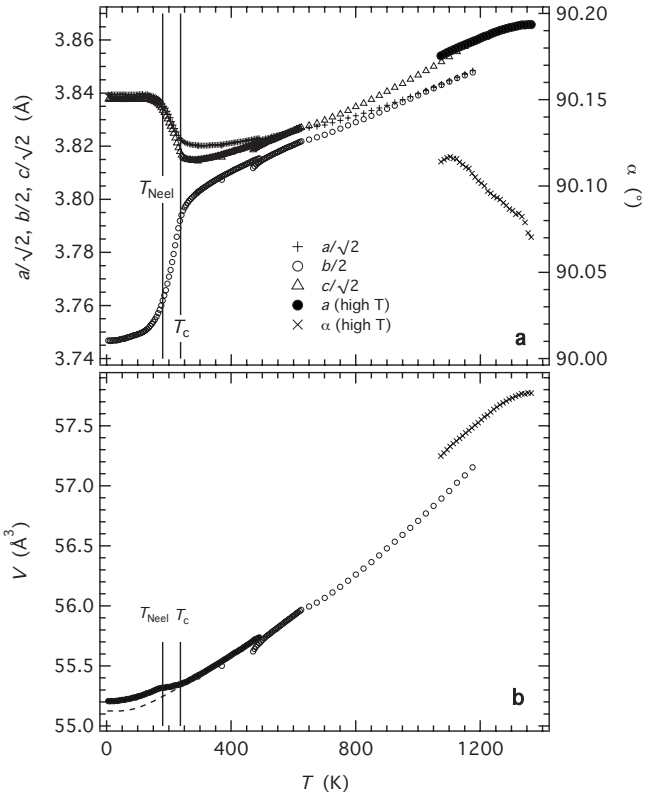

FIG. 2. Lattice parameter and volume variations in $Pr_{0.48}Ca_{0.52}MnO_3$ as a function of temperature, refined under *Pnma* or $R\bar{3}c$ symmetry. The highest temperature values of a and α are for the pseudocubic rhombohedral cell. The broken line in (b) is a fit of the baseline function given in the text to data for the *Pnma* structure between 300 and 490 K with the saturation temperature, Θ_{so}, fixed at 150 K.

to loss of oxygen in the vacuum at high temperatures. Diffraction patterns from the final high-temperature data set (1373–1073 K) were consistent with the presence of a predominant phase with $R\bar{3}c$ symmetry, although there was some reappearance of the *Pnma* phase below about 1173 K, to a maximum of about 15 wt % at 1073 K. For the purposes of this study, the patterns were analyzed on the basis of a single $R\bar{3}c$ phase. These data appear to be consistent with a transition $R\bar{3}c \leftrightarrow Pnma$ which is first order in character and has significant hysteresis between ~1100 and ~1200 K, though this aspect of the overall transformation behavior is not considered further in this paper. A room-temperature spectrum collected after cooling from 1373 K was consistent with *Pnma* symmetry but had even smaller peak splitting and weaker M-point reflections than after heating to 1173 K.

Variations in lattice parameters for the entire temperature interval are given in terms of the primitive cubic dimension in Fig. 2. They show the relatively sharp decrease in b and increase in a and c between ~250 and ~160 K described elsewhere for similar materials,[22–24] though with much higher resolution. At ±0.0001, statistical errors on the lattice parameters from the fitting are smaller than the size of the symbols in Fig. 2. The high resolution permits detection of a small but well-defined change in trend of unit-cell volume

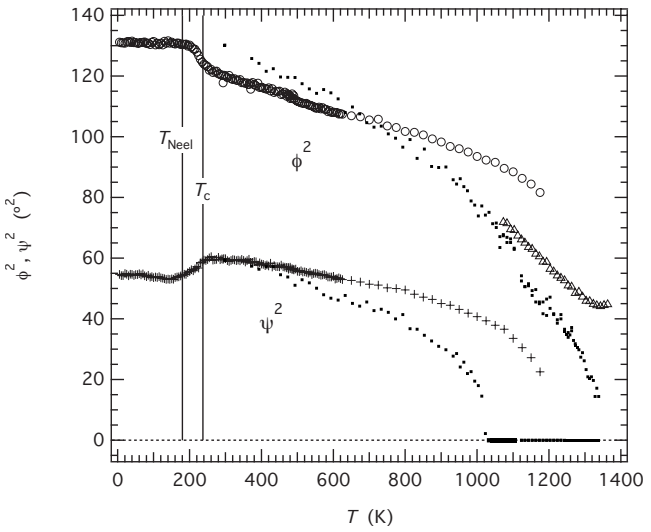

FIG. 3. Octahedral tilt angles determined from refined atomic coordinates of the average *Pnma* structure. Triangles are data for the high-temperature rhombohedral structure in $R\bar{3}c$. Dots are data for $SrZrO_3$ from McKnight *et al.* (Ref. 37).

through the same temperature range. Slight offsets in temperature and/or lattice parameters, evident between the two data sets in the range between room temperature and 490 K where they overlap, are presumed to be due to a change in systematic errors associated with the absolute scaling of lattice dimensions, or with the temperature determinations between the cryostat and furnace, or both. Data from the highest temperature run are from refinements under $R\bar{3}c$ symmetry.

Following the procedure described in detail in Carpenter *et al.*,[36] the extent of tilting of the octahedra about cubic [011] and [100] directions, corresponding to R-(ϕ°) and M-point (ψ°) tilts, respectively, has been estimated from the refined atomic coordinates of the *Pnma* structure. These are given as ϕ^2 and ψ^2 in Fig. 3, for later comparison with tilting in $SrZrO_3$. Small and continuous variations are evident through the 170–250 K interval, with more or less constant values below this and nonlinear decreases above. Tilt angles about [111] for the $R\bar{3}c$ structure were calculated using the formula given in Howard *et al.*,[74] and are also shown in Fig. 3.

Refined atomic coordinates have been used to determine average Mn-O bond lengths at temperatures up to 1175 K. In the *Pnma* structure there is only one symmetrically distinct MnO_6 octahedron and data for the three distinct bond lengths are shown in Fig. 4. Mn-O_1 lies approximately parallel to [010], while Mn-O_{21}, Mn-O_{22} lie approximately parallel to [101] and [10$\bar{1}$] respectively. Although there is some scatter in the data, the overall trends are clear. Above ~800 K, the bond lengths are the same and the octahedra have effectively cubic geometry. Between ~800 and ~240 K, two of the Mn-O bond lengths reduce and one of the bonds in the (010) plane lengthens. This arrangement has the same pattern as the M_2^+ ordering scheme of *Pnma* structures with Jahn-Teller distortions. At ~240 K, the two short bonds start to diverge steeply, due to reduction in the Mn-O_1 distance and increase

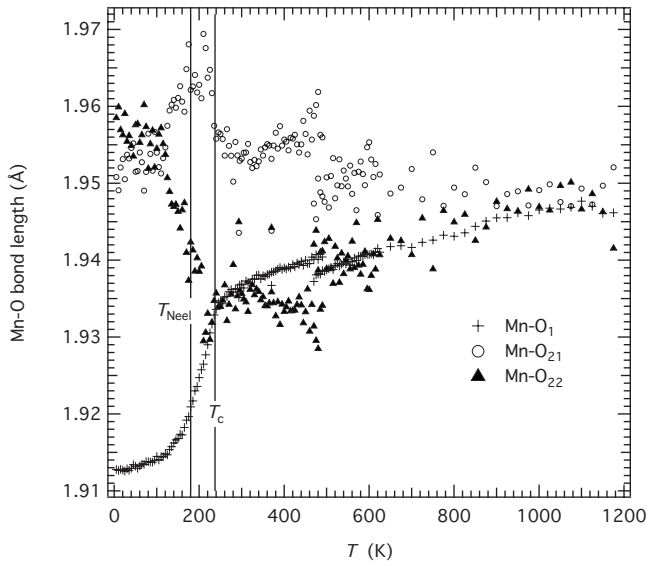

FIG. 4. Mn-O bond lengths determined from refined atomic coordinates of the average *Pnma* structure. Mn-O_1 is aligned approximately parallel to [010] while Mn-O_{21}, Mn-O_{22} lie approximately within the (010) plane.

in the Mn-O_{22} distance. The longest bond (Mn-O_{21}) shows an initial increase at the same temperature but then converges to the same value as the Mn-O_{22} bond at and below ~120 K. It should be noted, of course, that these bond lengths are averages for the low-temperature structure, as refined under *Pnma* symmetry. In principle a $Pnm2_1$ structure would allow for two distinct octahedra with 12 distinct Mn-O bond lengths in all.[61]

A distinctive feature of the diffraction patterns collected at temperatures below ~260 K is the development of markedly asymmetric line broadening. This is seen clearly in Fig. 5, which includes stacked segments of the patterns. The pairs of reflections near $d=1.9$ and 2.3 Å each diverge with falling temperature but also show additional intensity between them from ~250 to ~170 K, as would be characteristic of intensity from twin walls through a ferroelastic phase transition (e.g., Ref. 75). A quantitative measure of this broadening was obtained by fitting selected peaks with a pseudo-Voigt function, as described by Carpenter *et al.*[36] A typical result is shown in Fig. 6 for the pair of reflections with *d* spacings close to 1.9 Å, which are from (040) and (202) with respect to the *Pnma* cell but would merge to become (200) of the primitive cubic cell. There is a slight divergence of the two relatively narrow peaks on cooling toward ~250 K. Accompanying the divergence in *d* spacings between ~250 and ~160 K [Fig. 6(a)] is a steep increase and then decrease in the line widths with a maximum at ~210 K [Fig. 6(b)]. Below ~160 K a trend of slightly increasing line width with falling temperature, as established above ~260 K, is resumed. A slight asymmetry in the peak shapes is maintained down to the lowest temperature (Fig. 5). By way of contrast some of the other diffraction peaks appear to remain sharp, though peak fitting reveals that, in detail, this is not the case. The peak at ~2.2 Å corresponds to (111) of the parent cubic phase and becomes (022)+(220) of the *Pnma* structure. The *d* spacing [Fig. 6(c)] and peak width at half height [Fig. 6(d)] both show displacements in the ~260–170 K interval, which could be due to line broadening of the individual peaks or, more simply, to changes in the relative positions of the two peaks. The peak width, in particular, shows steep changes in trend at ~235 and ~210 K.

B. Strain analysis and comparison with $SrZrO_3$

The cubic reference lattice parameter, a_o, should strictly be obtained by extrapolation from the stability field of the cubic phase but the approximation $a_o=V^{1/3}$, where *V* is the unit cell volume of the *Pnma* and $R\bar{3}c$ structures, can be used without serious loss of accuracy for the shear strains, e_{tx} and e_4. Variations in these strains, as calculated using Eqs. (4), (5), and (12)–(14) and the lattice parameter data shown in Fig. 2, are shown in Fig. 7. The magnitude of the tetragonal shear strain, e_{tx}, increases with falling temperature ahead of the phase transition and then shows a steep increase in the

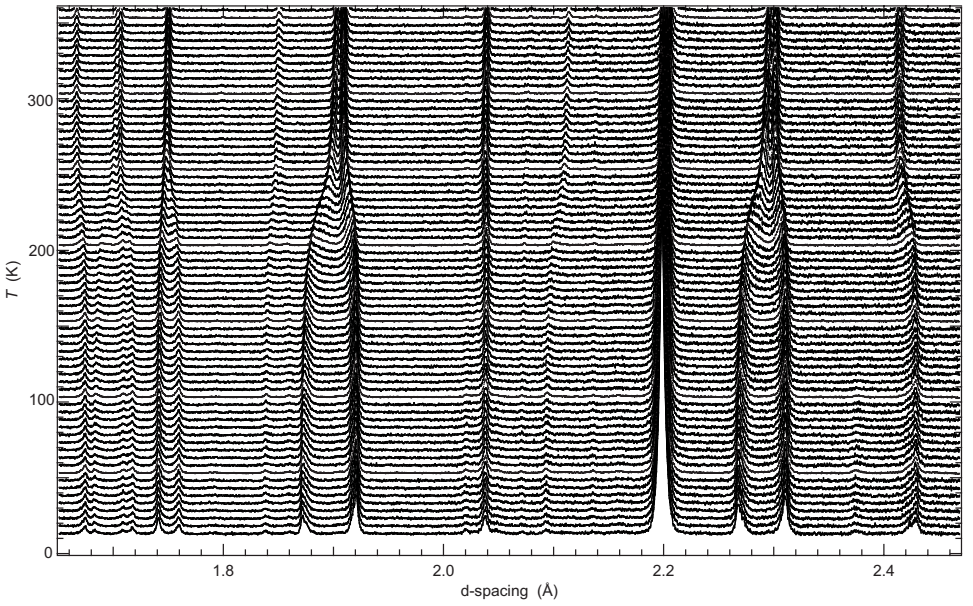

FIG. 5. Segments of neutron powder-diffraction patterns stacked according to the temperatures at which they were collected. Note the prominent asymmetric line broadening that develops just below the *Pnma*↔IC transition temperature of ~235 K. Some asymmetric broadening remains in the pattern collected at 10 K.

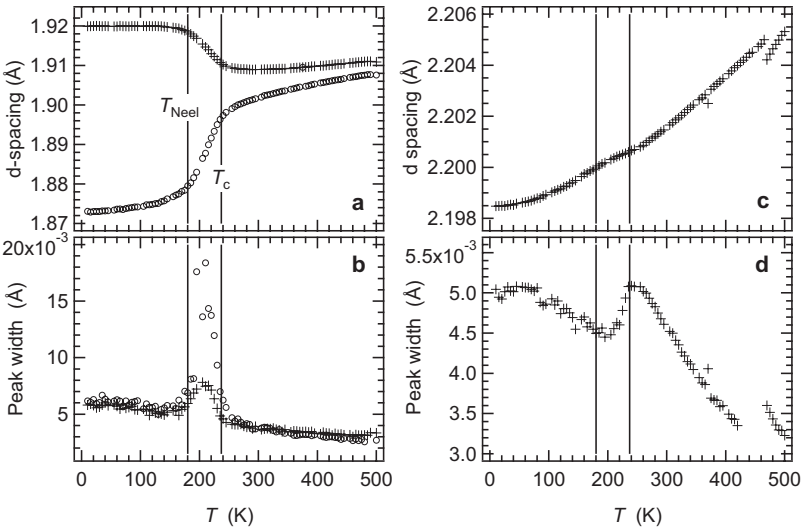

FIG. 6. Peak width and *d*-spacing variations with temperature of two representative peaks in powder-diffraction patterns. (a) and (b) are for 040 and 202 peaks, indexed under *Pnma* symmetry. (c) and (d) are for overlapping 022 and 220 reflections; changes in the apparent peak width are due to shifts in the positions of the individual peaks in this case.

250–170 K interval, before leveling off at low temperatures. In marked contrast, e_4 does not appear to anticipate the phase transition but shows a sharp change in trend at ~240 K before also leveling off at low temperatures. For the rhombohedral structure in the highest temperature data set, the shear strain, e_4, is given by $e_4 \approx \cos\alpha$ and shows declining values with increasing temperature indicative of the expected trend toward cubic symmetry.

The separate contributions of tilting and distortions of the MnO_6 octahedra to the shear strain e_{tx} [Eq. (10)] can be determined by comparison with the structural evolution of $SrZrO_3$, which does not contain a Jahn-Teller active cation. $SrZrO_3$ follows the transformation sequence $Pm\bar{3}m \leftrightarrow I4/mcm \leftrightarrow Imma \leftrightarrow Pnma$ with falling temperature.[76] Variations in the R-point and M-point tilt angles, $\phi°$ and $\psi°$ respectively, extracted from refinements of the neutron-diffraction data of Howard *et al.*[76] have been added to Fig. 3 and show a pattern of variation similar to the values obtained for $Pr_{0.48}Ca_{0.52}MnO_3$ below 1175 K. Variations in e_{tx} and e_4 from McKnight *et al.*[37] have been added to Fig. 7. In the case of $SrZrO_3$, both the R- and M-point tilting instabilities are close to tricritical in character. The similar pattern shown by the manganite tilt angles implies similar character, and differences are probably due to different critical temperatures, which must be higher for the manganite than for the zirconate.

In the *Pnma* structure of $SrZrO_3$, e_{tx} depends on only q_2 and q_4, with Eq. (10) reducing to

$$e_{tx} = -\frac{2(\lambda_3 q_2^2 - \lambda_4 q_4^2)}{\frac{1}{2}(C_{11}^o - C_{12}^o)}. \quad (18)$$

The order-parameter components and tilt angles are expected to evolve as $q_4 \propto \phi$ and $q_2 \propto \psi$. In both $SrZrO_3$ and $Pr_{0.48}Ca_{0.52}MnO_3$ the two tilt angles display rather similar trends, and Eq. (18) can be approximated conveniently as

$$e_{tx,tilt} = A[(1-x)\psi^2 - x\phi^2]. \quad (19)$$

Fitting the data for $SrZrO_3$ gives $x=0.35$, $A=-0.000096996$, which yields a good representation of the observed strain. Similar fitting to the data for $Pr_{0.48}Ca_{0.52}MnO_3$ gives a good representation of e_{tx}, with $x=0.4$ and $A=0.000098306$, but only for the temperature interval 775–1175 K. Below ~775 K, e_{tx} deviates substantially from the trend expected from octahedral tilting alone, as calculated using the average tilt angles given in Fig. 3. This difference, $\Delta e_{tx} = e_{tx} - e_{tx,tilt}$, is shown in Fig. 8 and provides a measure of the remaining order parameters, as [from Eq. (10)]

$$\Delta e_{tx} = -\left[\frac{2\lambda_{tM2+}q_{2JT}^2 + \lambda_{t\Gamma 3+}q_{tx} - 2\sqrt{3}\lambda_{t\Sigma 2}q_{\Sigma 2}^2}{\frac{1}{2}(C_{11}^o - C_{12}^o)}\right]. \quad (20)$$

Above ~775 K the average *Pnma* structure of $Pr_{0.48}Ca_{0.52}MnO_3$ is essentially the same as that of any normal tilted perovskite. Below ~775 K in the *Pnma* stability field, the pattern of Mn-O bond lengths implies a degree of M_2^+ ordering of uniaxially distorted octahedra similar to the

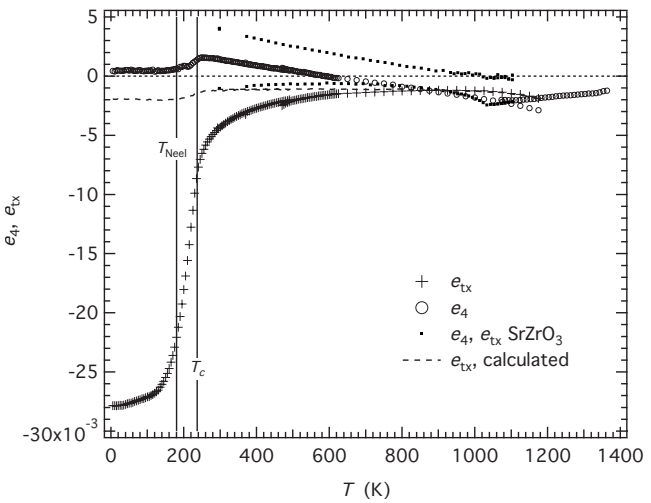

FIG. 7. Shear strains determined from the lattice parameter data shown in Fig. 2. The broken line represents e_{tx} arising from octahedral tilting alone. The tilting behavior of $Pr_{0.48}Ca_{0.52}MnO_3$ is closely similar to that of $SrZrO_3$, as shown by comparison with data from McKnight *et al.* (Ref. 37).

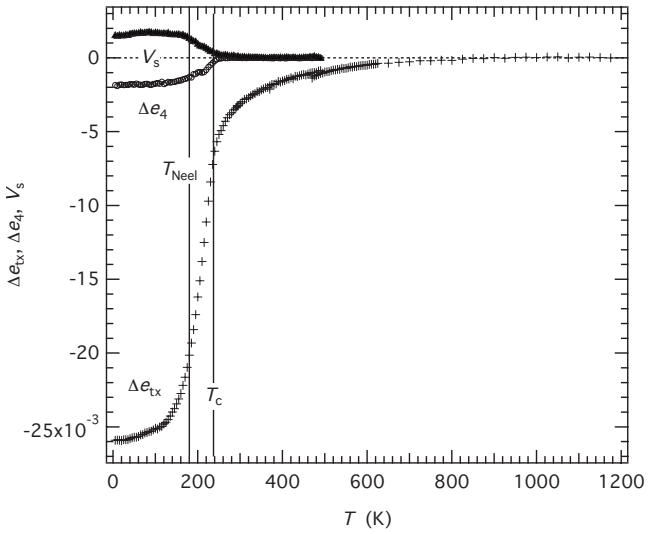

FIG. 8. Volume strain, V_s, and excess shear strain, Δe_4, due to the $Pnma \leftrightarrow$IC transition. Strain Δe_{tx} is the tetragonal shear strain after removal of the calculated contribution of octahedral tilting.

Jahn-Teller ordered structure of $LaMnO_3$, with little contribution from Γ_3^+ distortions. The increase in $|\Delta e_{tx}|$ below $\sim$775 K therefore defines the variation in q_{2JT}, with $q_{tx} \approx 0$. Note that the unit cell volume also appears to have a break in trend near $\sim$750 K (Fig. 2) which appears to indicate an increase in volume (positive volume strain) associated with the increase in q_{2JT}. This is also the same as occurs in association with Jahn-Teller ordering in $LaMnO_3$ (see Fig. 5 of Ref. 41). The largest contribution to Δe_{tx} is clearly associated with the transition at $\sim$235 K, when $q_{\Sigma 2}$ starts to contribute. The pattern of Mn-O bond lengths also changes, however, such that below $\sim$120 K the distorted octahedra have their unique axes aligned parallel to the crystallographic y axis, corresponding to $q_{2JT} \approx 0$, $q_{tx} \neq 0$. In the temperature interval $\sim$120–235 K there is a crossover between $q_{2JT} \approx 0$, $q_{tx} \neq 0$ and $q_{2JT} \neq 0$, $q_{tx} \approx 0$.

For a perovskite with tilting of undistorted octahedra, the orthorhombic shear strain e_4 is expected to vary with the order parameter for R-point tilting alone as, to good approximation

$$e_4 = -\frac{\lambda_5 q_4^2}{C_{44}^o}. \tag{21}$$

The observed variations in e_4 in $SrZrO_3$ (Ref. 37) and $(Ca,Sr)TiO_3$ (Ref. 35) do not show the expected relationship $e_4 \propto \phi^2$, however, which can be construed as implying that there is at least some degree of shearing of the octahedra. More importantly, e_4 is small at all temperatures in the *Pnma* stability field of $Pr_{0.48}Ca_{0.52}MnO_3$, implying that λ_5 is small. A degree of M_2^+ order would be expected to contribute to e_4 through the $\lambda_{eM2+M3+} q_{2JT} q_2$ term in Eq. (11) but there is no break in slope at $\sim$775 K and it appears that the coupling with q_{2JT} is weak ($\lambda_{eM2+M3+}$ small). On this basis, changes in e_4 below 235 K can be attributed almost exclusively to coupling with $q_{\Sigma 2}$. These have therefore been determined by first fitting $e_{4,o} = e_{4,1} + e_{4,2} \Theta_{se4} \coth(\Theta_{se4}/T)$ to data in the temperature range 250–490 K. The baseline saturation temperature is not tightly constrained by the data but the fit yields $\Theta_{se4} = 148 \pm 58$ K. The resulting variation of Δe_4, defined as $\Delta e_4 = e_4 - e_{4,o}$, is shown in Fig. 8 and provides information on the evolution of $q_{\Sigma 2}$ according to

$$\Delta e_4 = -\frac{2\lambda_{e1\Sigma 2} q_{\Sigma 2}^2}{C_{44}^o}. \tag{22}$$

The volume strain, V_s $[=(V-V_o)/V_o]$ $(=e_a$, to good approximation) for the low-temperature structure relative to the *Pnma* structure has been determined by first fitting the baseline saturation function $V_o = V_1 + V_2 \Theta_{so} \coth(\Theta_{so}/T)$ (following Refs. 77–81) to unit-cell volume data between 300 and 490 K [Fig. 2(b)]. The baseline saturation temperature, Θ_{so}, was not tightly constrained by the data and was therefore set at 150 K, following McKnight *et al.*[37] This yielded $V_1 = 58.866$, $V_2 = 0.0017294$ Å^3 as fit parameters, and the resulting temperature dependence of V_s shown in Fig. 8. The volume strain is positive, implying that the low temperature phase would be suppressed by increasing pressure. There are subtle breaks in trend at $\sim$180 and $\sim$85 K, the latter having been seen also in thermal expansion data for $Pr_{0.5}Ca_{0.5}MnO_3$.[82] $V_s = 0.0015$ at 10 K, which is in close agreement with the volume strain (0.0016) estimated by taking three times the difference in linear strain given by De Teresa *et al.*[83] between the ordered phase of $Pr_{2/3}Ca_{1/3}MnO_3$ in zero magnetic field and the disordered phase in a 12 T field.

If the strain behavior of the incommensurate structure can be represented in terms of coupling to a single order parameter, q_{IC}, the strains would be expected to be related in the typical manner for a coelastic transition as $V_s \propto \Delta e_4 \propto \Delta e_{tx} \propto q_{IC}^2$. Here q_{IC} represents the amplitude of the incommensurate modulation rather than the variations of $q_{\Sigma 2}$ within it. Figure 9(a) shows that Δe_4 and Δe_{tx} indeed scale linearly with V_s, apart from the additional contributions to Δe_{tx} at temperatures above the transition and the change in V_s below $\sim$85 K. An approximately linear trend is observed for the relationship between Δe_4 and Δe_{tx} below $\sim$260 K [Fig. 9(b)]. A better description would be two slightly different trends below and above 210 K but this is sensitive to the accuracy of the representation of the contribution to e_{tx} of octahedral tilting and is not reliable.

C. Thermodynamic character of the $Pnma \leftrightarrow$IC transition

The heat capacity anomaly reported by Cox *et al.*[49] through the temperature range $\sim$200–270 K, for a sample with the same composition as used in the present study, has its peak at 236 ± 1 K and is similar in form to the anomalies seen at phase transitions in anorthite, $CaAl_2Si_2O_8$ (Ref. 84) and lawsonite, $CaAl_2Si_2O_7(OH)_2.H_2O$ (Ref. 85) which are both tricritical in character. At low temperatures the Landau tricritical solution is

$$q^4 = \frac{a\Theta_s}{c}\left[\coth\left(\frac{\Theta_s}{T_c}\right) - \coth\left(\frac{\Theta_s}{T}\right)\right], \tag{23}$$

where a and c are coefficients for second-order and fourth-order terms in the Landau expansion, T_c is the transition

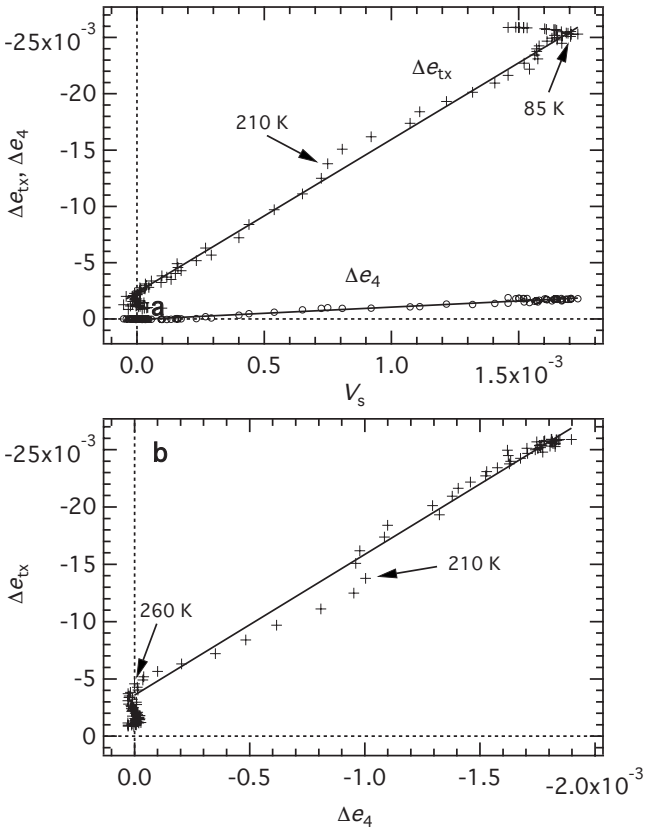

FIG. 9. Strain/strain relationships for strains arising at the $Pnma \leftrightarrow$IC transition and excluding the influence of octahedral tilting. Linear correlations are consistent with the expected relationships $V_s \propto \Delta e_4 \propto \Delta e_{tx} \propto q_{IC}^2$ with some precursor e_{tx} strain ahead of the transition point.

temperature and Θ_s is the order-parameter saturation temperature (e.g., Refs. 71, 77, 81, and 86). Based on the expectation $V_s \propto \Delta e_4 \propto \Delta e_{tx} \propto q_{IC}^2$ for coelastic properties, the variation in Δe_4^2 with temperature should then follow the right-hand side of Eq. (23). A fit to data between 5 and 235 K gives $T_c = 237 \pm 2$ K, $\Theta_s = 276 \pm 32$ K and provides a good description of the strain evolution (Fig. 10). V_s^2 follows Δe_4^2, perhaps with a small deviation near 180 K and a marked deviation below ~85 K (Fig. 10). Δe_{tx} scales with Δe_4 within reasonable experimental uncertainty [Fig. 9(b)]. The macroscopic strains are thus consistent with the $Pnma \leftrightarrow$IC transition being close to tricritical in character with some additional relaxation affecting the evolution of the volume strain.

V. DISCUSSION

Although the local instabilities triggering changes of structure in manganite solid solutions might be electronic, their effects are manifest as macroscopic strains which evolve in the same way as for any other phase transition driven by soft phonon modes. In classic cases such as α-β quartz, the actual symmetry-breaking mechanism is responsible for only a rather small proportion of the total energy change and the overwhelming contribution is due to the

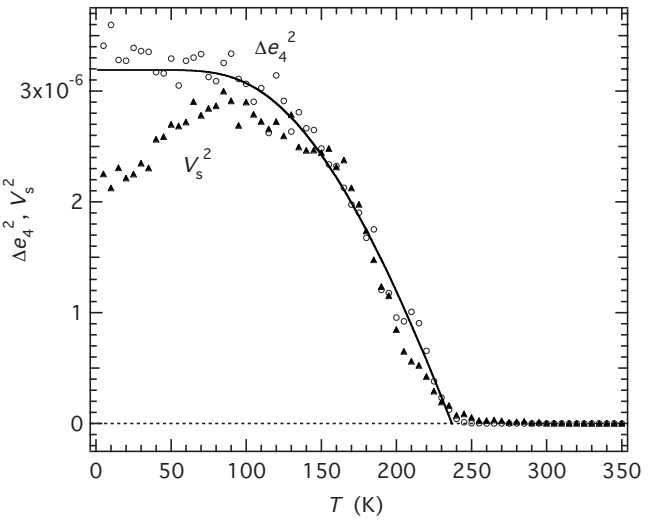

FIG. 10. Variation with temperature of (strains) (Ref. 2) which are expected to scale as q_{IC}^4. The solid line is a fit of an equation with the from of Eq. (23), showing that the $Pnma \leftrightarrow$IC transition can be described as Landau tricritical with $T_c = 237$ K, $\Theta_s = 276$ K.

coupled elastic strain relaxations.[33,87] In feldspars, coupling of individual order parameters with strains provides a mechanism for strong coupling between different order parameters and leads also to patterns of evolution which can be understood entirely from the perspective of Landau theory (e.g., Refs. 32, 33, and 88). The approach and results presented above appear to confirm that this straightforward model applies equally to $Pr_{0.48}Ca_{0.52}MnO_3$. Use of symmetry-adapted strains and a detailed consideration of how they are permitted to couple with different symmetry-breaking order parameters leads to a view of the structural evolution in terms of order parameters alone, as shown in Fig. 11.

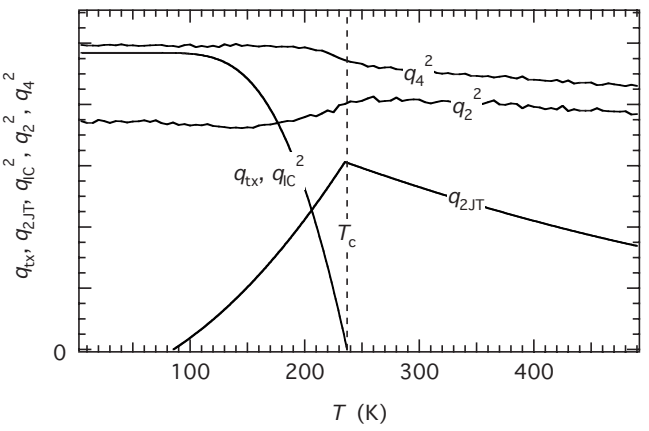

FIG. 11. Schematic variations in the principal order parameters through the $Pnma \leftrightarrow$IC transition. q_2 and q_4 are tilting order parameters and q_{tx}, q_{2JT} refer to two different Jahn-Teller ordering schemes, Γ_3^+ and M_2^+, respectively. The incommensurate order parameter, q_{IC}, scales with q_{tx} as $q_{IC}^2 \propto q_{tx}$. Below T_c there is a crossover between the two Jahn-Teller ordering schemes of deformed octahedra. This is accompanied by changes in the tilt angles.

The high-temperature behavior of $Pr_{0.48}Ca_{0.52}MnO_3$ is dominated by octahedral tilting which appears to be no different from the standard R+M-point tilting of octahedra in the (non-Jahn Teller) phase $SrZrO_3$. At some higher temperature there are probably two phase transitions: $Pnma \leftrightarrow R\bar{3}c$ (first order, and possibly in the temperature interval ~1100–1200 K) and $R\bar{3}c \leftrightarrow Pm\bar{3}m$. A degree of M_2^+ order develops continuously below ~775 K but Γ_3^+ order, also permitted in space group *Pnma*, does not. Symmetry breaking at the $Pnma \leftrightarrow$ IC transition is represented by the appearance of the Σ_2 order parameter (with gradient coupling between its two components) but is marked also by an increase in Γ_3^+ order and a decrease in M_2^+ order. From the variation of e_4 the development of the IC order parameter can be represented as being close to tricritical in character. Additional relaxations associated with the other secondary irreps of space group $Pnm2_1$ may well occur, including ferroelectric displacements due to Γ_4^- and Γ_5^-. (These might be extracted from higher quality data for atomic coordinates using the approach set out by Knight[89]). Coupling between the order parameters could be indirect through their individual coupling with strains or it could be direct. Whichever is the case, Fig. 11 reveals that effective coupling of Σ_2 with Γ_3^+ and R_4^+ components is favorable, whereas coupling with M_2^+ and M_3^+ components is unfavorable. By way of contrast, there is only the slightest hint of a strain relaxation (in the volume strain) accompanying the antiferromagnetic ordering transition known to occur at ~180 K. The implication is that this could be essentially independent of the other order parameters.

Treatment of the symmetry-adapted strains in this way does not permit overt discrimination between structural models such as checkerboard, bistripe and Zener polaron ordering, or of alternative descriptions based on charge density waves.[49,90,91] From a thermodynamic perspective, however, the transition appears to be close to tricritical and this could be due either to renormalization of the fourth-order Landau coefficient by strain/order-parameter coupling of the form λqe^2 or by contributions from configurational entropy in a transition which tends toward the order/disorder limit, as opposed to being purely displacive (e.g., see Ref. 92). The excess entropy of ~1.4 J mole^{-1} K^{-1} estimated for the $Pnma \leftrightarrow$ IC transition in $Pr_{0.48}Ca_{0.52}MnO_3$ from measurements of excess heat capacity by Cox *et al.*[49] is still substantially away from the order/disorder limit of R ln 2 =5.8 J mole^{-1} K^{-1}.

A. Microstructure

The pattern of line broadening in the primary powder-diffraction patterns through the temperature interval ~150–260 K is similar to that reported for $La_{0.5}Ca_{0.5}MnO_3$ through the temperature interval 180–250 K by Radaelli *et al.*[65] Selected pairs of peaks from patterns collected at 150, 200, 215, and 250 K are shown in Fig. 12 and can be compared with Fig. 2 of Radaelli *et al.*[65] The asymmetric line broadening at 150 K invariably occurs between pairs of reflections which would have identical *d* spacings in the parent cubic phase: (202) and (040) [Fig. 12(a)], (031) and (112)+(211) [Fig. 12(b)] as indexed for the *Pnma* cell. Above ~260 K, the bulk sample is structurally homogeneous, as it is again below ~150 K. In the intermediate temperature range it contains phases with a spread of different lattice spacings and these could be either as heterogeneous regions within individual grains or as discrete grains. The former could be due to the influence of transformation twins and the latter to the influence of grain size on transformation temperature, for example.

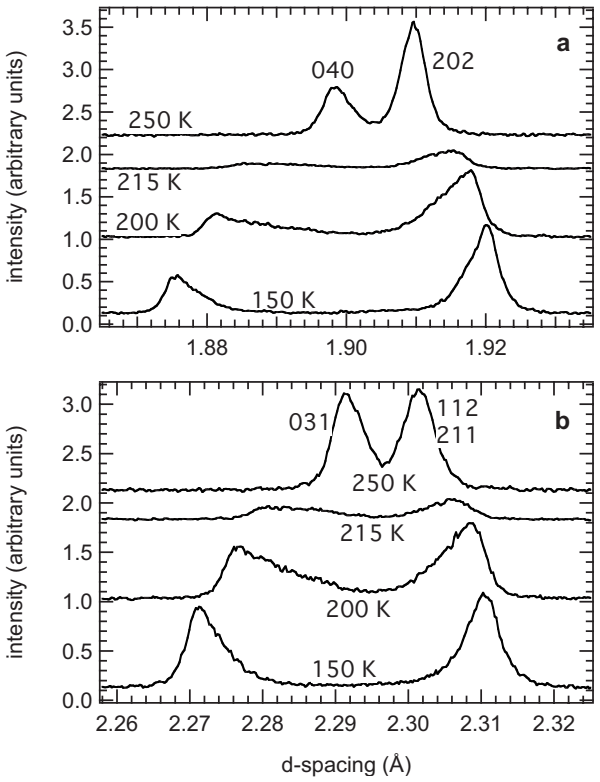

FIG. 12. Details of peak shapes for selected reflections at different temperatures through the $Pnma \leftrightarrow$ IC transition. Intermediate temperatures are marked by strong asymmetric line broadening. Indexing is for the *Pnma* lattice.

As the transition point of a second-order ferroelastic transition is approached from below, the twin wall thickness, *w*, increases as $w \propto (T_c - T)^{-1}$ and the contribution of the twin walls to the diffraction pattern is seen as an increase in intensity between twin-related pairs of reflections.[73,93–95] Transformation twins would not normally be expected to arise at the $Pnma \leftrightarrow$ IC transition but the room-temperature *Pnma* parent structure of $La_{0.33}Ca_{0.67}MnO_3$ already contains abundant $90°/m\{100\}$ and $120°/m\{110\}$ twins, which can be understood as having arisen from the symmetry loss with respect to $Pm\bar{3}m$ due to octahedral tilting.[96] Jooss *et al.*[64] have asserted that all of the six possible twin domain orientations are present with domain sizes of <100 nm in comparable Pr,Ca manganites (see, also, Ref. 30). The orientation of tilting changes between domains and, in principle, the tilt angles could go to zero at the center of each twin wall. Thus the $Pnma \leftrightarrow$ IC transition takes place in a material which is already structurally heterogeneous with respect to the order parameters which determine the stable phase. The same ar-

gument has been applied in relation to ferromagnetic ordering at twin walls by Chapman *et al.*[18]

If the IC structure occurs independently of the tilting, it should develop uniformly across an individual crystal with only minor disruption at the twin walls where the orientation of the IC direction changes. At the other extreme of strong coupling between the tilting and IC order parameters, the twin walls will have significantly different transformation characteristics in comparison with the domains themselves. Variations in tilt angles below ~235 K evident in Fig. 3, show that coupling indeed occurs between the tilt and IC order parameters. Direct coupling between these, labeled here generically as q_{tilt} and q_{IC}, is biquadratic in form $(\lambda q_{\text{IC}}^2 q_{\text{tilt}}^2)$, and for different values of static tilt angles this would give changes in the transition temperature as

$$T_c^* = T_c - \frac{2\lambda q_{\text{tilt}}^2}{a}, \tag{24}$$

where a is the standard coefficient for the second-order term in a Landau free energy expansion. If the overall coupling is favorable (λ negative), the domains would transform at a higher temperature than the walls but if it is unfavorable (λ positive), the twin walls would have a higher transition temperature. In the interval between the limiting transition temperatures of the domains and the centers of the domain walls, individual walls would have gradients in both IC and tilt order parameters and a concomitant range of lattice parameters. On this basis, the temperature dependence of line broadening shown in Fig. 6(b) implies such an interval of ~150–260 K. Details of the structure of the twin walls will depend both on the order parameter coupling and on the length scale of strain fields which arise from the contrast in lattice parameters between the domains and the centers of the twin walls.

At ~3% (Fig. 7), the total strain of the metrically tetragonal IC structure is comparable with that of many proper ferroelastic materials. For such large strains, an advantageous transformation mechanism might be simply to nucleate new 120° twin domains of the low-temperature structure in the parent *Pnma* phase, as occurs at the first-order transition in $Bi_{0.2}Ca_{0.8}MnO_3$.[72] Even at a second-order transition, the energy contribution of coupling between q_t and q_{IC} might become sufficient to stabilize domain walls with respect to the domain, in which case new walls could grow. At the very least, fluctuations in the tilt order parameter could be enhanced and structural heterogeneity within the domains could be amplified. Similar arguments could be made for order-parameter gradients through antiphase boundaries arising from the tilting transitions. Strain related variations in properties at both twin walls and antiphase boundaries have been explored more generally by Ahn *et al.*[97,98]

It is known that the transition temperature for the equivalent transition in $La_{1-x}Ca_xMnO_3$ reduces with reducing grain size (e.g., Refs. 99 and 100). The transition appears to be fully suppressed in $Pr_{0.5}Ca_{0.5}MnO_3$ with grain sizes of less than ~50 nm.[56,57] This effect can be understood in terms of changes in electronic structure between the surface layer and the core of a grain or, alternatively, simply as change in strain relaxation behavior with grain size.[17,56,57,99,100] The latter mechanism shows up in the influence of grain size on the structural transition in quartz.[101–103] With falling temperature, the onset of the transition is lower for smaller grains, giving a spread of lattice parameters for different grains in the bulk sample. At some lower temperature, the transition would be complete in all grains, so that they would all end up, once again, with essentially the same lattice parameters. In both $La_{0.25}Ca_{0.75}MnO_3$ and $La_{0.5}Ca_{0.5}MnO_3$ the shift in T_c only starts to exceed a few degrees once the grain size falls below ~150 nm (Fig. 12 of Ref. 99 and Fig. 7 of Ref. 100) and in $Pr_{0.5}Ca_{0.5}MnO_3$ the same change is seen below ~70 nm (Fig. 8 of Ref. 56). At the smaller grain sizes, the lattice parameters of the low-temperature structures of $La_{0.25}Ca_{0.75}MnO_3$, $La_{0.5}Ca_{0.5}MnO_3$, and $Pr_{0.5}Ca_{0.5}MnO_3$ also become significantly different,[56,57,100] however, and line broadening in diffraction patterns from a bulk sample containing a range of grain sizes would certainly occur. This does not match the present observations, though a slight asymmetry in peak shapes remains down to 10 K.

The possibility of twin walls being responsible for structural heterogeneities through the *Pnma*↔IC transition does not appear to have been investigated by transmission electron microscopy although clear evidence for the influence of twin walls on ferromagnetic ordering has been observed in $La_{0.25}Pr_{0.375}Ca_{0.375}MnO_3$ by magnetic force microscopy.[29] Wu *et al.*[30] reported the coexistence of *Pnma* and ordered phases over a wide temperature interval in $Pr_{1-x}Ca_xMnO_3$ but the intergrowths were found at room temperature, well above the transition point, and at 80 K, well below the transition point. Doping of $Pr_{1-x}Ca_xMnO_3$ with 2% Co in place of Mn produces asymmetric line broadening at 15 K which Yaicle *et al.*[104] have interpreted as being due to phase separation, though the distribution of two phases within grains or between grains is not known. A similar result has been obtained by doping with 1% Ti.[105]

B. Correlation of macroscopic strain with other physical properties

If the well-known changes in properties that accompany phase transitions in manganite solid solutions are directly related to changes in structure, they should also correlate with changes in macroscopic strain. Data in the literature all seem to be for temperatures below room temperature so no correlation of properties can be made for the onset of M_2^+ Jahn-Teller order below ~800 K. There are distinct pretransitional effects, however. The onset of a tail in the heat capacity occurs at ~260 K (Ref. 49) and a change in the trend of magnetization occurs at ~255 K (Refs. 49 and 50) which correlate with the onset of line broadening [Fig. 6(b)], the onset of a positive volume strain (Fig. 2) and the onset of changes in the octahedral tilt angles (Fig. 3). The peak in heat capacity at ~236 K (Ref. 49) is within experimental uncertainty of the *Pnma*↔IC transition temperature deduced from the evolution of e_4 (Fig. 10) and the onset of a divergence between average Mn-O_1 and Mn-O_{22} bond lengths (Fig. 4). This also is essentially the point at which the electrical resistivity starts to increase in $Pr_{0.5}Ca_{0.5}MnO_3$.[23] The

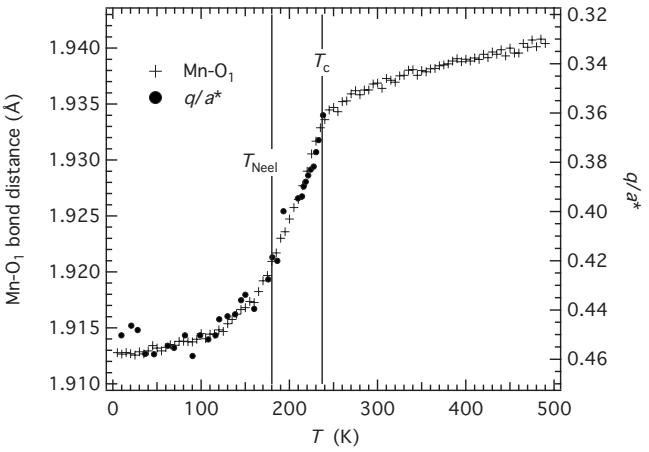

FIG. 13. Comparison of the repeat distance of the IC structure, as expressed through the parameter q/a^* [data of Sánchez *et al.* (Ref. 50)] with the Mn-O_1 bond length. The temperature dependences are indistinguishable, implying that the repeat length of the IC structure depends essentially on geometrical factors.

maximum in line broadening occurs at ~210 K [Fig. 6(b)] which correlates with the temperature at which the rate of change of lattice parameters reaches a maximum. The only possible change in physical properties which might correlate with this point is the ferroelectric or antiferroelectric phase transition proposed by Lopes *et al.*[67] to occur at ~20–30 K below the $Pnma \leftrightarrow$IC transition in $Pr_{1-x}Ca_xMnO_3$ samples with other compositions. The Néel temperature for $Pr_{0.5}Ca_{0.5}MnO_3$ is ~180 K (Refs. 23, 43, 47, 48, 51, and 52) but this appears in the strain evolution only as a barely detectable change in trend of the volume strain (Figs. 2, 8, and 10). The octahedral tilt angles revert to a more normal pattern at ~160 K and the end of line broadening is at ~140 K. There is perhaps a small change in slope of the heat capacity curve at ~130 K.[49]

There are also clear correlations between structural parameters, strains and the variation in the repeat distance of the incommensurate structure. Sánchez *et al.*[50] described the IC superlattice of $Pr_{0.48}Ca_{0.52}MnO_3$ in terms of q/a^*, where q here is the distance between a sublattice reflection and a superlattice reflection, and a^* is the reciprocal dimension of the sublattice. As shown in Fig. 13, their data for the temperature dependence of q/a^* are indistinguishable from the variation in the Mn-O_1 bond length. In turn, the Mn-O_1 bond length has been interpreted in terms of q_{tx}, the Γ_3^+ order parameter. Between T_c and ~120 K, the contribution of M_2^+ Jahn-Teller order goes to zero (Fig. 4), the contribution of Γ_3^+ increases and the incommensurate repeat distance reduces. Saturation of q/a^* at ~0.45–0.46 coincides with $q_{2JT} \rightarrow 0$ and saturation of q_{tx}. In other words, the IC repeat distance varies when the ratio of $M_2^+:\Gamma_3^+$ ordering varies but becomes fixed when q_{tx} is constant and q_{2JT} goes to zero. As an aside, it can also be noted that coupling of the IC structure to e_{tx}, via q_{tx}, means that variations in q/a^* would be induced by application of a uniaxial stress parallel to [010], or by a homogeneous stress within the (010) plane. Cox *et al.*[19] obtained small changes in q/a^* by inducing small strain variations within the (010) plane.

The rather small deviation in volume strain observed at ~85 K (Fig. 8 and 10) is quite similar in form to the change in linear thermal expansion observed for $Pr_{0.5}Ca_{0.5}MnO_3$ (Ref. 82) but does not so obviously match up with anomalies in other properties, though there are changes in magnetic properties which could be related. For example, Radaelli *et al.*[8] identified a ferromagnetic contribution from Pr developing below ~65 K in $Pr_{0.65}Ca_{0.35}MnO_3$. An increase in magnetization below ~50 K has been reported by Cox *et al.*[49] and Sánchez *et al.*[50] for $Pr_{0.48}Ca_{0.52}MnO_3$, and has been attributed to a reentrant spin glass transition in $Pr_{0.5}Ca_{0.5}MnO_3$.[55] The transition from antiferromagnetic order to a canted antiferromagnetic structure at ~125 K in $Pr_{0.65}Ca_{0.35}MnO_3$ (Ref. 106) can probably be ruled out on the basis that Tonogai *et al.*[107] found the transition temperature to reduce rapidly with increasing Ca content.

In terms of cause and effect, the changes in heat capacity and magnetic properties just above the $Pnma \leftrightarrow$IC transition can clearly be understood in terms of typical pretransitional fluctuations which occur at most structural phase transitions. Changes in electrical resistivity coincide more precisely with the actual transition temperature, and hence with establishment of long-range order. Line broadening is interpreted above in terms of thickening of preexisting transformation twin walls to give a structurally heterogeneous material through the temperature interval 260–140 K. It remains to be determined whether the possible ferroelectric behavior reported by Lopes *et al.*[67] is related particularly to the existence of thick twin walls. Changes in the magnetic properties, on the other hand, seem to be associated with only small changes in the volume strain, suggesting very weak magnetostriction.

Continuous variations in elastic properties from a polycrystalline sample of $Pr_{1-x}Ca_xMnO_3$ through the $Pnma \leftrightarrow$IC transition[108] are consistent with the transition being thermodynamically continuous. Hazama *et al.*[109,110] show sharp discontinuities in the elastic properties of a single crystal of $Pr_{0.5}Ca_{0.5}MnO_3$, however, perhaps suggesting a role for grain size in determining the thermodynamic character of the transition. By analogy with the case of quartz,[103] suppression of strain/order-parameter coupling with reducing grain size would reduce renormalization of the Landau fourth-order coefficient and cause a crossover from first order to tricritical. Common features to the elastic properties are softening $[(C_{11}-C_{12})$ in the single crystal case, longitudinal velocity for the ceramic] as the transition is approached from above, pretransitional softening above T_c and stiffening below T_c.[108,109]

C. A driving mechanism based on order-parameter coupling

Three separate order parameters have been used to account in detail here for the strain evolution of $Pr_{0.48}Ca_{0.52}MnO_3$. Coupling with the tilt order parameters gives small strains, typical of other perovskites such as $SrZrO_3$. Coupling with Jahn-Teller order parameters gives much larger strains. In the case of $LaMnO_3$, coupling with the M_2^+ order parameter gives values of e_4 and e_{tx} of up to ~4%, for example. The Γ_3^+ order parameter, q_{tx}, couples bi-

linearly with e_{tx} ($\lambda q_{tx} e_{tx}$), giving values of up to ~3%, and linear quadratically with e_4 ($\lambda q_{tx} e_4^2$), giving much smaller values of e_4 of <3‰ for the latter (Fig. 8). In framework silicates, coupling of individual order parameters with strains provides a mechanism for coupling between the order parameter themselves. The stability of the IC structure of $Pr_{0.48}Ca_{0.52}MnO_3$ can be interpreted in the same terms since strain coupling of individual order parameters leads to direct coupling of the form $\lambda q_2^2 q_{\Sigma 2}^2$, $\lambda q_4^2 q_{\Sigma 2}^2$, and $\lambda q_{tx} q_{\Sigma 2}^2$.

In principle, the IC structure could develop simply by gradient coupling between the two components of the Σ_2 irrep and the possible contribution of these gradient terms has been referred to previously (e.g., Ref. 9). However, IC phases do not appear to develop in manganites without any tilts or which have only R-point tilting, such as when Sr is substituted for Ca in $La_{1-x}Ca_xMnO_3$ or $Pr_{1-x}Ca_xMnO_3$.[23,48,111–118] Thus the biquadratic coupling of $q_{\Sigma 2}$ with both q_2 (M_2^+) and q_4 (R_4^+) seems to be important even though the tilting instabilities occur at much higher temperatures. Contributions from irreps M_2^+ and Γ_3^+ are also implicated since a small degree of M_2^+ Jahn-Teller ordering develops within the *Pnma* structure below ~800 K but is replaced by Γ_3^+ below the *Pnma*↔IC transition point. In this context, the phase transition actually has the characteristics of a pseudoproper ferroelastic transition driven by q_{tx}. The bilinear coupling of q_{tx} with e_{tx} would cause elastic softening ahead of the transition according to

$$(C_{11} - C_{12}) = (C_{11} - C_{12})^{o}\left(\frac{T - T_c^*}{T - T_c}\right), \tag{25}$$

where $(C_{11}-C_{12})$ is the observed elastic constant, $(C_{11}-C_{12})^o$ is the elastic constant excluding the influence of the phase transition. T_c^* is the transition point and T_c is the critical temperature, which is lower than T_c^* by an amount that depends on the square of the strain/order-parameter coupling coefficient.[89,119,120] This form of softening has indeed been observed in $Pr_{0.5}Ca_{0.5}MnO_3$ (single crystal: Hazama *et al.*;[109,110] polycrystalline sample: Zheng *et al.*,[108] and Chen *et al.*[121]). Below the transition point, the bilinear coupling leads to stiffening of $(C_{11}-C_{12})$,[110] again as would be expected for pseudoproper ferroelastic behavior.

Equation (25) gives $(C_{11}-C_{12}) \rightarrow 0$ at $T=T_c^*$ but the *Pnma*↔IC transition occurs before this point is reached due to the onset of the Σ_2 order parameter, $q_{\Sigma 2}$. Strong coupling of the form $\lambda q_{tx} q_{\Sigma 2}^2$ should give $q_{tx} \propto q_{\Sigma 2}^2$, and assigning strains $\Delta e_{tx} \propto q_{tx}$, $\Delta e_4 \propto q_{\Sigma 2}^2$ leads to the expectation $\Delta e_{tx} \propto \Delta e_4$, as is observed to reasonable approximation [Fig. 9(b)]. Thus the phase transition itself is defined by coupling between two order parameters with separate instabilities. The symmetry-breaking mechanism ($q_{\Sigma 2}$) probably contributes only a small proportion of the total energy change which is actually dominated by the contributions of q_{tx} and its coupling with e_{tx}.

This pattern of order-parameter coupling would also stabilize the commensurate $Pnm2_1$ structure. In the end-member phase of plagioclase feldspar, $CaAl_2Si_2O_8$ (anorthite), a continuous transition from incommensurate to commensurate order can be observed and the relative stability of the two structures is due to the stability of their antiphase boundaries.[31,122,123] These are stabilized within the solid solution by coupling to a second order parameter so that the IC structure consists of homogeneous domains separated by boundaries which have steep order-parameter gradients. The equivalent $Pr_{1-x}Ca_xMnO_3$ structure would have domains with relatively homogeneous q_{tx} and $q_{\Sigma 2}$ separated by antiphase boundaries with steep order-parameter gradients. Gradient terms in the two $q_{\Sigma 2}$ components presumably provide the initial symmetry-breaking mechanism for the IC structure but coupling with the tilt and Jahn-Teller order parameters could again account for a substantial proportion of the stabilization energy. Radaelli *et al.*[65] already argued that there is strong coupling between the modulation and octahedral tilt pattern, as would be formalized in terms of $\lambda q_2^2 q_{\Sigma 2}^2$, $\lambda q_4^2 q_{\Sigma 2}^2$ coupling effects which show up in the variations in average tilt angles through the *Pnma*↔IC transition. Insights into the structural context of this coupling is provided by the recent geometric simulation of Sartbaeva *et al.*,[124] from which it is clear that local frustration effects arising from misfits between adjacent MnO_6 octahedra with different distortions can be accommodated effectively by changes in octahedral tilting. The close correlation between the IC repeat distance and variations of the M_2^+ and Γ_3^+ order parameters further enforces the view that the IC structure can be thought of structurally in terms of geometrical fitting of deformed MnO_6 octahedra assisted by tilting, and thermodynamically in terms of strain/order-parameter coupling.

VI. CONCLUSIONS

The symmetry and strain analysis presented here provides a formalized description of both the coupling between different aspects of the structural evolution of $Pr_{1-x}Ca_xMnO_3$ that have been described qualitatively, for example, by Jirák *et al.*,[23] and the widely recognized role of strain in determining the structural and physical properties of manganite solid solutions. Specifically: (1) important structural features which stabilize the IC structure can be attributed to the separate contributions of order parameters related to the irreducible representations M_3^+, R_4^+, M_2^+, Γ_3^+, and Σ_2 of space group $Pm\bar{3}m$, and coupling between them. These correspond physically to two different octahedral tilt systems, two different Jahn-Teller ordering schemes and charge order or Zener polaron ordering, respectively. (2) From the evolution with temperature of symmetry-adapted strains and other structural data, it has been shown that the Jahn-Teller ordering scheme with M_2^+ symmetry, as in $LaMnO_3$, starts to develop below ~775 K. This gives way at the $Pm\bar{3}m$↔IC phase transition to a different ordering scheme, in which the unique axis of individual distorted octahedral are aligned in the same direction (Γ_3^+). (3) Symmetry breaking at the *Pnma*↔IC transition is driven by the Σ_2 order parameter but this couples favorably with R-point tilting and Γ_3^+ Jahn Teller order and unfavorably with M-point tilting and M_2^+ Jahn-Teller order. The coupling mechanism is probably through separate coupling of each with common strains. (4) The *Pnma*↔IC transition is accompanied by large shear strains (up to ~0.025)

and a small volume strain (up to ~0.0015). The shearing arises primarily from bilinear coupling of the tetragonal shear strain with the Γ_3^+ Jahn-Teller order parameter which, in turn, is coupled to the driving (Σ_2) order parameter. It is likely that the main energy reduction arises from Γ_3^+ Jahn Teller ordering and shear strain relaxation, rather than from Σ_2 order (charge or Zener polaron ordering) by itself. Bilinear coupling of Γ_3^+ Jahn-Teller ordering with the tetragonal shear strain is responsible for softening of shear elastic constants as the transition is approached from both high and low temperatures (pseudoproper ferroelastic character). (5) Treating the overall behavior of $Pr_{0.48}Ca_{0.52}MnO_3$ from the perspective of elastic strain relaxations reveals that the $Pnma \leftrightarrow$IC transition conforms to a standard tricritical pattern of order-parameter evolution derived from Landau theory, i.e., $q^4 \propto (T_c - T)$, with $T_c = 237 \pm 2$ K. This is in spite of the local, electronic origin of the transition and is due to the long ranging correlation length of the order parameters from their coupling with strain. (6) Given that there is strong coupling between the different order parameters and strain on a macroscopic length scale, it is inevitable that there will also be strain variations associated with order-parameter gradients locally within the IC structure. The incommensurate repeat distance of $Pr_{0.48}Ca_{0.52}MnO_3$ follows the average Γ_3^+ Jahn-Teller order parameter monotonically as a function of temperature below T_c, and it is likely that strain gradients at the antiphase boundaries are accommodated by variations in M-point and R-point tilting. (7) In marked contrast with tilting and Jahn-Teller distortions, antiferromagnetic ordering appears to be coupled with strain only to the slightest degree, if at all. As a consequence, it does not influence tilting or distortions of the octahedra to any obvious extent. There is, however, a definite change in trend for the volume strain below ~85 K which could be due to additional changes in magnetic structure. (8) The presence of ferroelastic twins due to the octahedral tilting transitions means that changes in structure and properties of $Pr_{0.48}Ca_{0.52}MnO_3$ occur in crystals which are structurally heterogeneous. Line broadening in a temperature interval around T_c (~150–260 K) is consistent with thickening of these twin walls and could imply differences in structural evolution and/or transition temperature between the walls and the matrix. (9) A general consequence of strong coupling between order parameters and strain, recognized for macroscopic length scales and locally associated with microstructure, is that variations in any one of the order parameters in the proximity of defects, around impurity atoms, at local strain fields due to cation disordering or within homogeneous regions, must enhance the propensity of these materials to develop heterogeneity on a nanoscale. (10) Finally, while the present focus has been on the evolution of Γ_3^+, M_2^+, M_3^+, R_4^+, and Σ_2 order parameters, Table III reveals that a number of other relaxations are allowed under $Pnm2_1$ symmetry which could give rise to additional instabilities. The phenomenological richness of these materials may not yet have been fully explored.

ACKNOWLEDGMENTS

Support from the Leverhulme Foundation and from the Australian Research Council (Grant No. DP0877695) is gratefully acknowledged.

[1] M. B. Salamon and M. Jaime, Rev. Mod. Phys. **73**, 583 (2001).
[2] *Nanoscale Phase Separation and Colossal Magnetoresistance*, edited by E. Dagotto (Springer, Berlin, New York, 2002), p. 456.
[3] A.-M. Haghiri-Gosnet and J.-P. Renard, J. Phys. D **36**, R127 (2003).
[4] *Colossal Magnetoresistive Manganites*, edited by T. Chatterji (Kluwer Academic, Dordrecht, 2004), p. 447.
[5] Y. Tokura, Rep. Prog. Phys. **69**, 797 (2006).
[6] C. Israel, M. J. Calderón, and N. D. Mathur, Mater. Today **10**, 24 (2007).
[7] P. K. Siwach, H. K. Singh, and O. N. Srivastava, J. Phys.: Condens. Matter **20**, 273201 (2008).
[8] P. G. Radaelli, G. Iannone, D. E. Cox, M. Marezio, H. Y. Hwang, and S.-W. Cheong, Physica B **241-243**, 295 (1998).
[9] F. Zhong and Z. D. Wang, Phys. Rev. B **61**, 3192 (2000).
[10] N. D. Mathur and P. B. Littlewood, Solid State Commun. **119**, 271 (2001).
[11] Z. Q. Li, X. H. Zhang, J. S. Yu, X. J. Liu, X. D. Liu, H. Liu, P. Wu, H. L. Bai, C. Q. Sun, J. J. Lin, and E. Y. Jiang, Phys. Lett. A **325**, 430 (2004).
[12] G. C. Milward, M. J. Calderón, and P. B. Littlewood, Nature (London) **433**, 607 (2005).
[13] I. Kézsmárki, Y. Tomioka, S. Miyasaka, L. Demkó, Y. Okimoto, and Y. Tokura, Phys. Rev. B **77**, 075117 (2008).
[14] J. P. Attfield, Chem. Mater. **10**, 3239 (1998).
[15] R. Y. Gu and C. S. Ting, Phys. Rev. B **65**, 214426 (2002).
[16] A. R. Bishop, T. Lookman, A. Saxena, and S. R. Shenoy, Europhys. Lett. **63**, 289 (2003).
[17] M. J. Calderón, A. J. Millis, and K. H. Ahn, Phys. Rev. B **68**, 100401(R) (2003).
[18] J. P. Chapman, J. P. Attfield, L. M. Rodriguez-Martinez, L. Lezama, and T. Rojo, Dalton Trans. **2004**, 3026.
[19] S. Cox, E. Rosten, J. C. Chapman, S. Kos, M. J. Calderón, D.-J. Kang, P. B. Littlewood, P. A. Midgley, and N. D. Mathur, Phys. Rev. B **73**, 132401 (2006).
[20] S. Cox, J. C. Loudon, A. J. Williams, J. P. Attfield, J. Singleton, P. A. Midgley, and N. D. Mathur, Phys. Rev. B **78**, 035129 (2008).
[21] T. Z. Ward, J. D. Budai, Z. Gai, J. Z. Tischler, L. Yin, and J. Shen, Nat. Phys. **5**, 885 (2009).
[22] M. T. Fernández-Díaz, J. L. Martínez, J. M. Alonso, and E. Herrero, Phys. Rev. B **59**, 1277 (1999).
[23] Z. Jirák, F. Damay, M. Hervieu, C. Martin, B. Raveau, G. André, and F. Bourée, Phys. Rev. B **61**, 1181 (2000).
[24] X. G. Li, R. K. Zheng, G. Li, H. D. Zhou, R. X. Huang, J. Q. Xie, and Z. D. Wang, Europhys. Lett. **60**, 670 (2002).
[25] M. Uehara, S. Mori, C. H. Chen, and S.-W. Cheong, Nature (London) **399**, 560 (1999).

[26] K. H. Ahn, T. Lookman, and A. R. Bishop, Nature (London) **428**, 401 (2004).
[27] D. N. Argyriou, U. Ruett, C. P. Adams, J. W. Lynn, and J. F. Mitchell, New J. Phys. **6**, 195 (2004).
[28] V. B. Shenoy, D. D. Sarma, and C. N. R. Rao, ChemPhysChem **7**, 2053 (2006).
[29] W. Wu, C. Israel, N. Hur, S. Park, S.-W. Cheong, and A. de Lozanne, Nature Mater. **5**, 881 (2006).
[30] L. Wu, R. F. Klie, Y. Zhu, and Ch. Jooss, Phys. Rev. B **76**, 174210 (2007).
[31] M. A. Carpenter, in *Feldspars and Their Reactions*, NATO ASI Series C Vol. 421, edited by I. Parsons (Kluwer, Dordrecht, 1994), p. 221.
[32] E. K. H. Salje, Phys. Rep. **215**, 49 (1992).
[33] M. A. Carpenter, E. K. H. Salje, and A. Graeme-Barber, Eur. J. Mineral. **4**, 621 (1998).
[34] M. A. Carpenter, Rev. Mineral. Geochem. **39**, 35 (2000).
[35] M. A. Carpenter, A. I. Becerro, and F. Seifert, Am. Mineral. **86**, 348 (2001).
[36] M. A. Carpenter, C. J. Howard, K. S. Knight, and Z. Zhang, J. Phys.: Condens. Matter **18**, 10725 (2006).
[37] R. E. A. McKnight, C. J. Howard, and M. A. Carpenter, J. Phys.: Condens. Matter **21**, 015901 (2009).
[38] C. J. Howard, Z. Zhang, M. A. Carpenter, and K. S. Knight, Phys. Rev. B **76**, 054108 (2007).
[39] M. A. Carpenter, C. J. Howard, B. J. Kennedy, and K. S. Knight, Phys. Rev. B **72**, 024118 (2005).
[40] M. A. Carpenter and C. J. Howard, Acta Crystallogr., Sect. B: Struct. Sci. **65**, 134 (2009).
[41] M. A. Carpenter and C. J. Howard, Acta Crystallogr., Sect. B: Struct. Sci. **65**, 147 (2009).
[42] C. J. Howard and M. A. Carpenter, Acta Crystallogr., Sect. B: Struct. Sci. **66**, 40 (2010).
[43] C. Martin, A. Maignan, M. Hervieu, and B. Raveau, Phys. Rev. B **60**, 12191 (1999).
[44] J. P. Hill, C. S. Nelson, M. v. Zimmermann, Y.-J. Kim, D. Gibbs, D. Casa, B. Keimer, Y. Murakami, C. Venkataraman, T. Gog, Y. Tomioka, Y. Tokura, V. Kiryukhin, T. Y. Koo, and S.-W. Cheong, Appl. Phys. A: Mater. Sci. Process. **73**, 723 (2001).
[45] M. v. Zimmermann, C. S. Nelson, J. P. Hill, D. Gibbs, M. Blume, D. Casa, B. Keimer, Y. Murakami, C.-C. Kao, C. Venkataraman, T. Gog, Y. Tomioka, and Y. Tokura, Phys. Rev. B **64**, 195133 (2001).
[46] Z. Jirák, C. Martin, M. Hervieu, and J. Hejtmánek, Appl. Phys. A: Mater. Sci. Process. **74**, s1755 (2002).
[47] Z. Jirák, S. Krupička, Z. Šimša, M. Dlouhá, and S. Vratislav, J. Magn. Magn. Mater. **53**, 153 (1985).
[48] S. Krupicka, M. Marysko, Z. Jirák, and J. Hejtmánek, J. Magn. Magn. Mater. **206**, 45 (1999).
[49] S. Cox, J. C. Lashley, E. Rosten, J. Singleton, A. J. Williams, and P. B. Littlewood, J. Phys.: Condens. Matter **19**, 192201 (2007).
[50] D. Sánchez, M. J. Calderón, J. Sánchez-Benítez, A. J. Williams, J. P. Attfield, P. A. Midgley, and N. D. Mathur, Phys. Rev. B **77**, 092411 (2008).
[51] R. Kajimoto, T. Kakeshita, Y. Oohara, H. Yoshizawa, Y. Tomioka, and Y. Tokura, Phys. Rev. B **58**, R11837 (1998).
[52] R. Kajimoto, H. Yoshizawa, Y. Tomioka, and Y. Tokura, Phys. Rev. B **63**, 212407 (2001).
[53] M. v. Zimmermann, J. P. Hill, D. Gibbs, M. Blume, D. Casa, B. Keimer, Y. Murakami, Y. Tomioka, and Y. Tokura, Phys. Rev. Lett. **83**, 4872 (1999).
[54] A. Trokiner, A. Yakubovskii, S. Verkhovskii, A. Gerashenko, and D. Khomskii, Phys. Rev. B **74**, 092403 (2006).
[55] G. Cao, J. Zhang, S. Wang, J. Yu, C. Jing, S. Cao, and X. Shen, J. Magn. Magn. Mater. **301**, 147 (2006).
[56] T. Zhang and M. Dressel, Phys. Rev. B **80**, 014435 (2009).
[57] Z. Jirák, E. Hadová, O. Kaman, K. Knížek, M. Maryško, E. Pollert, M. Dlouhá, and S. Vratislav, Phys. Rev. B **81**, 024403 (2010).
[58] H. T. Stokes, D. M. Hatch, and B. J. Campbell, ISOTROPY http://stokes.byu.edu/isotropy.html (2007).
[59] A. Daoud-Aladine, J. Rodríguez-Carvajal, L. Pinsard-Gaudart, M. T. Fernández-Díaz, and A. Revcolevschi, Appl. Phys. A: Mater. Sci. Process. **74**, s1758 (2002).
[60] A. Daoud-Aladine, J. Rodríguez-Carvajal, L. Pinsard-Gaudart, M. T. Fernández-Díaz, and A. Revcolevschi, Phys. Rev. Lett. **89**, 097205 (2002).
[61] R. J. Goff and J. P. Attfield, Phys. Rev. B **70**, 140404(R) (2004).
[62] M. Giot, P. Beran, O. Pérez, S. Malo, M. Hervieu, B. Raveau, M. Nevriva, K. Knizek, and P. Roussel, Chem. Mater. **18**, 3225 (2006).
[63] H. T. Stokes, D. M. Hatch, and H. M. Nelson, Phys. Rev. B **47**, 9080 (1993).
[64] Ch. Jooss, L. Wu, T. Beetz, R. F. Klie, M. Beleggia, M. A. Schofield, S. Schramm, J. Hoffmann, and Y. Zhu, Proc. Natl. Acad. Sci. U.S.A. **104**, 13597 (2007).
[65] P. G. Radaelli, D. E. Cox, M. Marezio, and S.-W. Cheong, Phys. Rev. B **55**, 3015 (1997).
[66] D. V. Efremov, J. Van den Brink, and D. I. Khomskii, Nature Mater. **3**, 853 (2004).
[67] A. M. L. Lopes, J. P. Araújo, V. S. Amaral, J. G. Correia, Y. Tomioka, and Y. Tokura, Phys. Rev. Lett. **100**, 155702 (2008).
[68] M. Hervieu, A. Maignan, C. Martin, N. Nguyen, and B. Raveau, Chem. Mater. **13**, 1356 (2001).
[69] M. Hervieu, S. Malo, O. Perez, P. Beràn, C. Martin, G. Baldinozzi, and B. Raveau, Chem. Mater. **15**, 523 (2003).
[70] G. Subías, J. García, P. Beran, M. Nevřiva, M. C. Sánchez, and J. L. García-Muñoz, Phys. Rev. B **73**, 205107 (2006).
[71] M. A. Carpenter, Am. Mineral. **92**, 309 (2007).
[72] V. Podzorov, B. G. Kim, V. Kiryukhin, M. E. Gershenson, and S.-W. Cheong, Phys. Rev. B **64**, 140406(R) (2001).
[73] A. C. Larson and R. B. Von Dreele, Los Alamos National Laboratory Report No. LAUR 86–748, 2004 (unpublished).
[74] C. J. Howard, B. J. Kennedy, and B. Chakoumakos, J. Phys.: Condens. Matter **12**, 349 (2000).
[75] K. R. Locherer, S. A. Hayward, P. J. Hirst, J. Chrosch, M. Yeadon, J. S. Abell, and E. K. H. Salje, Philos. Trans. R. Soc. London, Ser. A **354**, 2815 (1996).
[76] C. J. Howard, K. S. Knight, B. J. Kennedy, and E. H. Kisi, J. Phys.: Condens. Matter **12**, L677 (2000).
[77] E. K. H. Salje, B. Wruck, and H. Thomas, Z. Phys. B **82**, 399 (1991).
[78] H.-W. Meyer, M. A. Carpenter, A. Graeme-Barber, P. Sondergeld, and W. Schranz, Eur. J. Mineral. **12**, 1139 (2000).
[79] H.-W. Meyer, S. Marion, P. Sondergeld, M. A. Carpenter, K. S. Knight, S. A. T. Redfern, and M. T. Dove, Am. Mineral. **86**, 566 (2001).
[80] P. Sondergeld, W. Schranz, A. V. Kityk, M. A. Carpenter, and E. Libowitzky, Phase Transitions **71**, 189 (2000).

[81] M. A. Carpenter, H.-W. Meyer, P. Sondergeld, S. Marion, and K. S. Knight, Am. Mineral. **88**, 534 (2003).
[82] M. Doerr, G. Reményi, M. Rotter, S. Sahling, M. Saint-Paul, and M. Loewenhaupt, J. Magn. Magn. Mater. **290-291**, 906 (2005).
[83] J. M. De Teresa, M. R. Ibarra, C. Marquina, P. A. Algarabel, and S. Oseroff, Phys. Rev. B **54**, R12689 (1996).
[84] E. K. H. Salje, in *Physical Properties and Thermodynamic Behaviour of Minerals*, NATO ASI Series C Vol. 225, edited by E. K. H. Salje (Reidel, Dordrecht, 1988), p. 75.
[85] J.-M. Martín-Olalla, S. A. Hayward, H.-W. Meyer, S. Ramos, J. Del Cerro, and M. A. Carpenter, Eur. J. Mineral. **13**, 5 (2001).
[86] J. M. Pérez-Mato and E. K. H. Salje, J. Phys.: Condens. Matter **12**, L29 (2000).
[87] M. A. Carpenter, in *Energy Modelling in Minerals*, edited by C. M. Gramaccioli, EMU Notes in Mineralogy Vol. 4 (Eötvös University Press, Budapest, 2002), p. 311.
[88] M. A. Carpenter and E. K. H. Salje, Eur. J. Mineral. **10**, 693 (1998).
[89] K. S. Knight, Can. Mineral. **47**, 381 (2009).
[90] J. C. Loudon, S. Cox, N. D. Mathur, and P. A. Midgley, Philos. Mag. **85**, 999 (2005).
[91] S. Cox, J. Singleton, R. D. McDonald, A. Migliori, and P. B. Littlewood, Nature Mater. **7**, 25 (2008).
[92] M. A. Carpenter, in *The Stability of Minerals*, edited by G. D. Price and N. L. Ross (Chapman and Hall, London, 1992), p. 172.
[93] S. A. Hayward, J. Chrosch, E. K. H. Salje, and M. A. Carpenter, Eur. J. Mineral. **8**, 1301 (1996).
[94] J. Chrosch and E. K. H. Salje, Physica C **225**, 111 (1994).
[95] J. Chrosch and E. K. H. Salje, J. Appl. Phys. **85**, 722 (1999).
[96] R. Wang, J. Gui, Y. Zhu, and A. R. Moodenbaugh, Phys. Rev. B **63**, 144106 (2001).
[97] K. H. Ahn, T. Lookman, A. Saxena, and A. R. Bishop, Phys. Rev. B **68**, 092101 (2003).
[98] K. H. Ahn, T. Lookman, A. Saxena, and A. R. Bishop, Phys. Rev. B **71**, 212102 (2005).
[99] T. Zhang, T. F. Zhou, T. Qian, and X. G. Li, Phys. Rev. B **76**, 174415 (2007).
[100] T. Sarkar, B. Ghosh, A. K. Raychaudhuri, and T. Chatterji, Phys. Rev. B **77**, 235112 (2008).
[101] N. A. Pertsev and E. K. H. Salje, Phys. Rev. B **61**, 902 (2000).
[102] S. Rios, E. K. H. Salje, and S. A. T. Redfern, Eur. Phys. J. B **20**, 75 (2001).
[103] R. E. A. McKnight, T. Moxon, A. Buckley, P. A. Taylor, T. W. Darling, and M. A. Carpenter, J. Phys.: Condens. Matter **20**, 075229 (2008).
[104] C. Yaicle, C. Frontera, J. L. García-Munoz, C. Martin, A. Maignan, G. André, F. Bourée, C. Ritter, and I. Margiolaki, Phys. Rev. B **74**, 144406 (2006).
[105] C. Frontera, J. L. García-Munoz, P. Beran, N. Bellido, I. Margiolaki, and C. Ritter, Chem. Mater. **20**, 3068 (2008).
[106] O. Yanagisawa, M. Izumi, W.-Z. Hu, K. Nakanishi, and H. Nojima, J. Supercond. **12**, 307 (1999).
[107] T. Tonogai, T. Satoh, K. Miyano, Y. Tomioka, and Y. Tokura, Phys. Rev. B **62**, 13903 (2000).
[108] R. K. Zheng, G. Li, Y. Yang, A. N. Tang, W. Wang, T. Qian, and X. G. Li, Phys. Rev. B **70**, 014408 (2004).
[109] H. Hazama, Y. Nemoto, T. Goto, Y. Tomioka, A. Asamitsu, and Y. Tokura, Physica B **312-313**, 757 (2002).
[110] H. Hazama, T. Goto, Y. Nemoto, Y. Tomioka, A. Asamitsu, and Y. Tokura, Phys. Rev. B **69**, 064406 (2004).
[111] F. Damay, C. Martin, M. Hervieu, A. Maignan, B. Raveau, G. André, and F. Bourée, J. Magn. Magn. Mater. **184**, 71 (1998).
[112] F. Damay, Z. Jirák, M. Hervieu, C. Martin, A. Maignan, B. Raveau, G. André, and F. Bourée, J. Magn. Magn. Mater. **190**, 221 (1998).
[113] F. Damay, C. Martin, A. Maignan, M. Hervieu, B. Raveau, Z. Jirák, G. André, and F. Bourée, Chem. Mater. **11**, 536 (1999).
[114] Z. Jirák, J. Hejtmánek, K. Knížek, M. Maryško, V. Šíma, and R. Sonntag, J. Magn. Magn. Mater. **217**, 113 (2000).
[115] A. Barnabé, M. Hervieu, C. Martin, A. Maignan, and B. Raveau, J. Phys. Chem. Solids **62**, 1365 (2001).
[116] C. Autret, C. Martin, M. Hervieu, A. Maignan, and B. Raveau, Chem. Mater. **15**, 1886 (2003).
[117] K. Knížek, J. Hejtmánek, Z. Jirák, C. Martin, M. Hervieu, B. Raveau, G. André, and F. Bourée, Chem. Mater. **16**, 1104 (2004).
[118] I. Dhiman, A. Das, P. K. Mishra, and L. Panicker, Phys. Rev. B **77**, 094440 (2008).
[119] R. Feile, A. Loidl, and K. Knorr, Phys. Rev. B **26**, 6875 (1982).
[120] K. Knorr, A. Loidl, and J. K. Kjems, Physica B **136**, 311 (1986).
[121] C. X. Chen, T. Qian, R. K. Zheng, F. Wang, and X. G. Li, Phys. Status Solidi B **241**, 1827 (2004).
[122] M. A. Carpenter, Am. Mineral. **76**, 1110 (1991).
[123] M. A. Carpenter, Am. Mineral. **76**, 1120 (1991).
[124] A. Sartbaeva, S. A. Wells, M. F. Thorpe, E. S. Bozin, and S. J. L. Billinge, Phys. Rev. Lett. **97**, 065501 (2006).